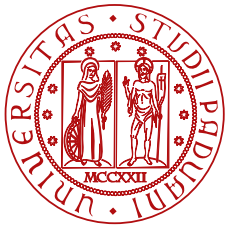

UNIVERSITÀ DEGLI STUDI DI PADOVA

ICEA

MASTER THESIS IN ENVIRONMENTAL ENGINEERING - ENVIRONMENT AND SUSTAINABILITY

3D geomechanical modeling for CO_2 geological storage in faulted reservoir

MASTER CANDIDATE

Teresa Biliato

Student ID 2040624

SUPERVISOR

Prof. Pietro Teatini

CO-SUPERVISOR

Dr. Andrea Franceschini

ACADEMIC YEAR
2022-2023

Abstract

CO_2 geological sequestration and injection in depleted gas or oil fields, also referred to as Carbon Capture and Storage (CCS), is one of the possibilities to reduce Greenhouse Gas (GHG) emissions, which would contribute to limit global warming and its effects. This methodology presents some geomechanical issues that must be properly addressed, especially when CO_2 is injected in faulted reservoirs. This thesis investigates the potential mechanical failure and land displacement for a depleted faulted reservoir in the northern Adriatic basin where CCS is planned to be activated within the next few years. The geomechanical response of a scenario addressing a preliminary CO_2 injection aimed at testing the storage effectiveness is investigated using the three-dimensional finite element-interface element geomechanical model GEPS3D. The mechanical failure could be represented by faults reactivation, leading the creation of a pathway for CO_2 to escape or inducing seismic events because of the fault sliding associated to the change of the local stress state. A sensitivity analysis to the main mechanical parameters of an elasto-visco-plastic constitutive relationship is carried out. The actual state of the reservoir and surrounding aquifers, i.e. the stress state characterizing the rock system after the end of the primary production and a few years of natural pressure recovery following the shutdown of the production wells, are also properly simulated by the same modeling approach and represent the initial condition for the scenario of CO_2 injection. Preliminary modeling analyses have also allowed to highlight that the static model of the reservoir provided by the oil company is characterized by elements with horizontal dimensions extremely larger than the vertical one. This geometric feature of the finite element grid precludes the accurate computation of the stress change on the fault planes due to CCS.

Contents

List of Figures

List of Tables

List of Acronyms

CCS Carbon Capture and Storage

CDR Carbon Dioxide Removal

EPRDM Elasto-Plastic Rate Dependent Model

EU European Union

FE Finite Elements

GEPS3D Geomechanical Elasto-Plastic 3D Simulator

GHG Greenhouse Gas

IEA International Energy Agency

IE Interface Elements

IPCC Intergovernmental Panel on Climate Change

OCR Overconsolidation Ratio

SSCM Soft Soil Creep Model

UNFCCC United Nations Framework Convention on Climate Change

1 Introduction

In the latest Report published by the Intergovernmental Panel on Climate Change (IPCC) in March 2023, it is stated that human activities are the *unequivocal* root of global warming, with a surface temperature that has risen of 1.1 °C compared to the levels of 1850-1900 [21]. In order to diminish the devastating effects of climate change, which would manifest on a global scale, some concrete actions must be taken.
Notwithstanding the fact that the first option to be considered must always be mitigation, consisting in the reduction of GHG emissions from their sources, evidence shows the necessity for approaches that combine mitigation, adaptation and remediation. One possibility that belongs to the latest category and which is increasingly being investigated is CCS.
According to the IPCC, a first definition of CCS can be described as:

> *Carbon dioxide (CO_2) capture and storage (CCS) is a process consisting of the separation of CO_2 from industrial and energy-related sources, transport to a storage location and long-term isolation from the atmosphere [1].*

CCS is a rapidly developing and already considerably studied technology, vital to reach a condition of net-zero emissions by 2050. In fact, most of the models cannot find a solution to stay below 1.5 °C without including Carbon Dioxide Removal (CDR) technologies such as CCS [27]. Particularly, it can be seen as extremely important for industrial sectors which are responsible for the production of a huge amount of emissions which are hard to abate, for instance

steel, iron or chemical sectors, and it is gaining much attention by international organizations such as the IPCC or the International Energy Agency (IEA). As stated by the Global CCS Institute in their five-year strategic plan for accelerating the development of this technique, around 80% of countries worldwide that have set the target of reaching carbon neutrality and contributing to the United Nations Framework Convention on Climate Change (UNFCCC) have recognized the role of CCS. It can be divided into different options, which consist in, for instance, ocean storage or underground geological repository, the latter of which is analysed in this thesis. The process is divided into capturing, transporting, usually throughout pipelines, and final injection into a deep rock formation. It got to the attention of the public in the 1990s, and the first performed dedicated project was in the North Sea in 1996 [27]. It can be performed both onshore and offshore, and in different geological settings, from depleted oil to gas fields, deep coal seams or saline formations.
One successful example is the In Salah CO_2 storage facility in Algeria, which has injected CO_2 from 2004 to 2011, with a total amount of 3.8 million tons of stored CO_2 and no reported leakage [4]. In the 2005 Special Report on CCS, the IPCC considered *likely* that 99% or more of the injected CO_2 will be retained for 1000 years, as it would be stored in depleted geologic formations previously containing fossil fuels. Moreover, CO_2 is usually injected at depths of about 1000 m or below, where it acquires a liquid-like density which allows for an effective utilization of the available underground space [2]. In order for a project to be carried out, a number of key questions must be asked, whether to assess its feasibility. It is actually fundamental for it to be feasible from an environmental, economic and technical point of view. These aspects lead to the choice of the possible injection site and further questions lead to a long-term stability assessment and continuous monitoring.

Another section that should be deeply analysed is the regulatory framework, which does not pertain to the scope of this thesis, but should always be considered and improved given the lack of clarity on, for instance, post injection responsibilities or long-term monitoring. The IEA describes the current situation and compares it with needed storage capacity when relating to the Net Zero Scenario of the IPCC, depicting a clearly unbalanced projection as shown in Figure 1.1. A more detailed state of the art is represented in Figure 1.2, with the current infrastructure development divided into regions and related to yearly injection capacity. The figure shows how North America has a more advanced

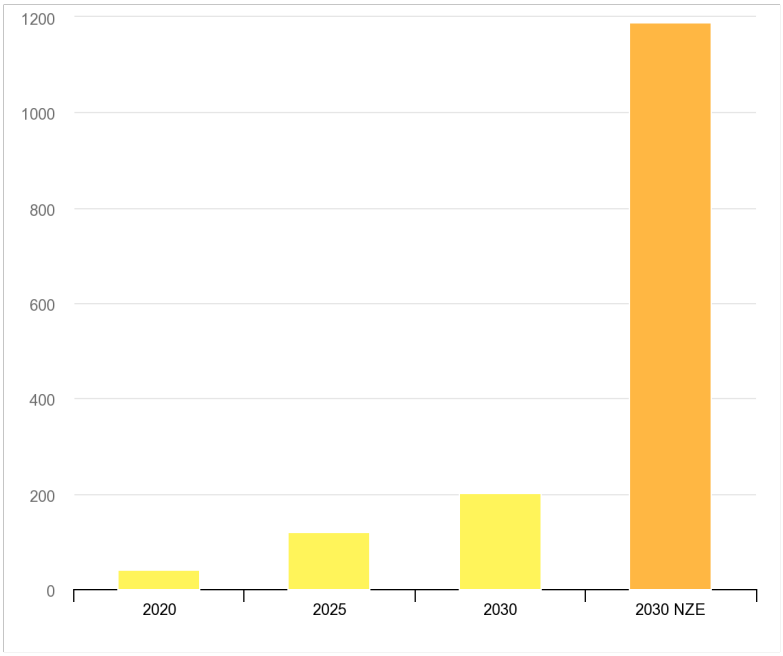

Figure 1.1: Annual CO_2 storage capacity [$MtCO_2/y$], current and planned vs Net Zero Scenario, 2020-2030. Adapted from [19].

development and operational settings of this technology, whilst Europe is still concentrating on assessing its feasibility.

In the European Union (EU) the development of dedicated infrastructures for CO_2 transport and storage is mentioned in the REGULATION (EU) 2022/869, of 30th May 2022 on the guidelines for trans-European energy infrastructure, amending Regulations (EC) No 715/2009, (EU) 2019/942 and (EU) 2019/943 and Directives 2009/73/EC and (EU) 2019/944, and repealing Regulation (EU) No 347/2013, although only generally described in Annex II [7]. This prospect overcomes the hurdles linked to the London Protocol, especially since it prohibited export of Carbon Dioxide with the purpose of offshore storage [8]. Nevertheless, storage assessment is a rather fundamental step for the development process of CCS, since resources need to match capacity and other criteria, such as geomechanical stability, which is here assessed.

The thesis falls within the scope of the analyses required in the planning of a CCS project. Specifically, this work is focused on investigating the geomechanical issues associated with a scenario of CO_2 injection in a faulted offshore reservoir located in the Northern Adriatic Sea, Italy. Notice that the importance of the geomechanical aspects and related processes is often underestimated but can have a primary role when the environmental impacts of CCS plans need to be

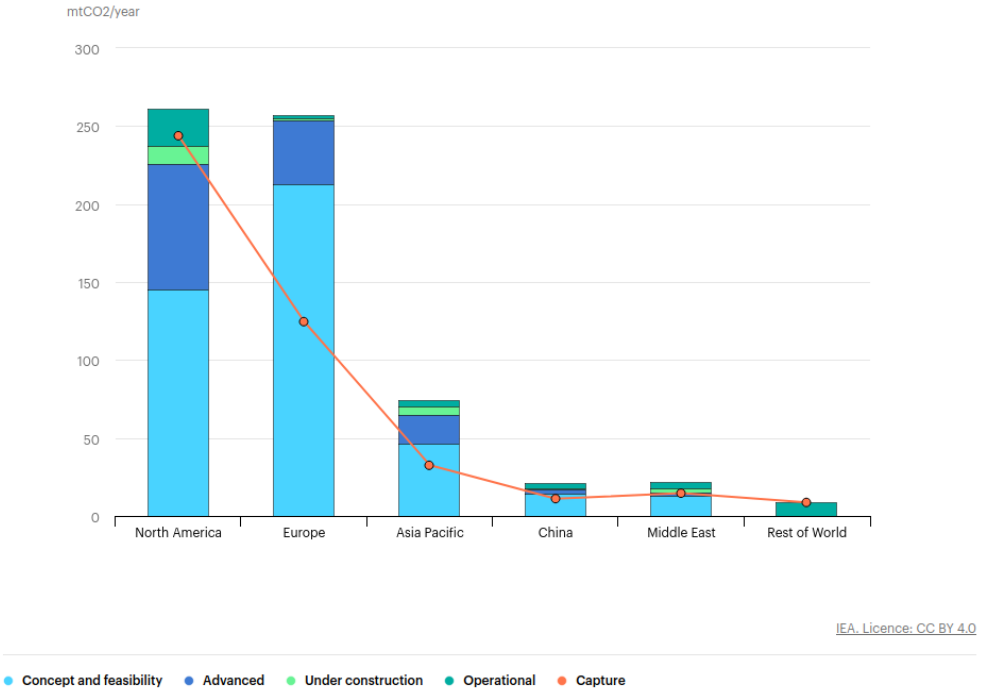

Figure 1.2: State of the art and development of CCS infrastructures on a global scale. Adapted from [19].

addressed. In fact, these aspects are fundamental when evaluating the long-term stability of a geological repository, especially in faulted basins, not only for the creation of possible pathways for the CO_2 to escape, but also for the possibility of inducing seismic events because of fault reactivation, or land vertical uplift [6, 10, 29].

In order to address these processes, modeling tools were necessary due to the complex formation of the site of interest. The analyses presented in this thesis are carried out by an advanced 3D geomechanical simulator, Geomechanical Elasto-Plastic 3D Simulator (GEPS3D). The simulator uses zero-thickness Interface Elements (IE) to simulate fault reactivation and forecast possible slippage and opening. Moreover, the simulations address the quantification of vertical and horizontal displacements during both the primary production of the reservoir occurred over the past decades and the planned injection of CO_2. It must be noted that the simulation of primary production is needed to characterize the stress field at the inception of the CO_2 injection. It is also useful in a carried out sensitivity analysis on the main parameters in the stress-strain relationship implemented to characterize the Northern Adriatic sedimentary deposits.

2

Theoretical Background

The geological storage of carbon dioxide involves many different processes and aspects, acting on wide spacial and temporal scales and impacting on both surface and subsurface. Depending on the location and the geomechanical properties of the site, these processes must be carefully investigated. The mathematical formulation of the problem is provided in the current chapter.

Another crucial aspect, which is just mentioned in the current study, is fluid dynamics. Since the void space not occupied by soil is filled with either gases or liquids, the movements and changes in pressure of these fluids have been studied in depth, as in cases reported in [5]. Flux and displacement occur simultaneously and should therefore be considered together, in what is called a coupled approach [23, 26]. However, this approach is complicated, also from a numerical perspective, and provides results which are similar to what is defined as uncoupled approach, where the pressure field is considered known a priori [15]. In this thesis, the uncoupled method is applied, with the pressure field computed with the use of a flow model.

2.1 Governing Equations

Soil can be seen as a porous medium, where solid phase and void space coexist. The latter, is usually interconnected and occupied by fluid phases, e.g. water and/or air in underground aquifers, together with gas or oil in hydrocarbon reservoirs. This configuration enables a movement of the fluids throughout the domain.

When the considered system is subject to changes driven, for instance, by the injection or withdrawal of fluids from the reservoir, this structure reacts with some deformations. The behavior and response of the ground to these events show a high level of complexity, but some assumptions that simplify its resolution prove to be useful in formulating the governing equations of the domain.

It is beneficial to provide the definition of the used quantities which often recur in the chapter, and which are of paramount importance for the problem description. Firstly, the effective stress tensor and its components can be described as:

$$\sigma = \begin{bmatrix} \sigma_{xx} & \tau_{yx} & \tau_{zx} \\ \tau_{xy} & \sigma_{yy} & \tau_{zy} \\ \tau_{xz} & \tau_{yz} & \sigma_{zz} \end{bmatrix} \tag{2.1}$$

The strain tensor ϵ is defined as:

$$\epsilon = \begin{bmatrix} \epsilon_{xx} & \epsilon_{yx} & \epsilon_{zx} \\ \epsilon_{xy} & \epsilon_{yy} & \epsilon_{zy} \\ \epsilon_{xz} & \epsilon_{yz} & \epsilon_{zz} \end{bmatrix} \tag{2.2}$$

With the two tensors being symmetric, they can both be rewritten as the following vectors, which will later be used, using the standard Voigt notation:

$$\boldsymbol{\sigma} = (\sigma_{xx}, \sigma_{yy}, \sigma_{zz}, \tau_{xy}, \tau_{yz}, \tau_{xz})^T \tag{2.3}$$

$$\boldsymbol{\epsilon} = (\epsilon_{xx}, \epsilon_{yy}, \epsilon_{zz}, \epsilon_{xy}, \epsilon_{xz}, \epsilon_{yz})^T \tag{2.4}$$

Finally, the displacement vector is expressed as $\mathbf{u} = (u, v, w)$.

One of the most commonly assumed simplifications in porous media is isotropy, meaning that mechanical properties can be considered orientation-independent. In fact, given the assumptions of isotropic and isothermal conditions, it can be stated that deformation in the domain is mainly driven by pore pressure and total displacement by rock compressibility, when considering small deformation. In a 3D spatial domain, called Ω, the quasi-static governing equations for mechanical equilibrium are:

$$\nabla \cdot \hat{\sigma} + \rho_b \mathbf{g} = 0 \tag{2.5}$$

where $\mathbf{g}$ is gravity, $\rho_b = \phi\rho_f + (1-\phi)\rho_s$ is the bulk density, ρ_f the total fluid density, ρ_s the solid phase density, ϕ the porosity and $\nabla\cdot$ the divergence operator. Finally, $\hat{\sigma}$ is the total stress, distinguishable from the effective stress thanks to the *hat* symbol. This is related to pressure and deformation from the following equation:

$$\hat{\sigma} - \hat{\sigma}_0 = \mathbb{C} : \epsilon - b(p_f - p_{f,0})\mathbf{1} \tag{2.6}$$

where $\mathbb{C}$ is the fourth order stiffness tensor of the solid matrix, the second order strain tensor ϵ, which can also be written as $\epsilon = (\nabla\mathbf{u} + \nabla^T\mathbf{u})/2$, with $\mathbf{u}$ the already defined displacement vector and ∇ the gradient operator, b is the Biot coefficient, and $\mathbf{1}$ is the second order identity tensor. The subscript 0, defines the reference state.

Fluid pressure p_f is defined by the following equation, considering both wetting and non-wetting phase, respectively the liquid and gas phases:

$$p_f = p_g - S_w(p_g - p_w) = S_g p_g + S_w p_w \tag{2.7}$$

The subscripts g and w refer to gas and water, as non-wetting and wetting phase respectively, and S represents the saturation index [29].

2.2 Poroelasticity theory

In a porous medium, the mechanics describing the behavior of the interactions between the different phases in the simplified assumption of elastic media is called poroelasticity. This theory was proposed by Biot in 1941 [3] with the aim at finding displacements, strains and stresses as representative values of the changes in volume. The responses in terms of surface and subsurface motion can be expressed in both vertical and horizontal displacements, and are independent of the loading history. This means that there is a unique stress-strain relation, where the medium returns to a relaxed state whenever the applied loads are removed [28].

In reservoir geomechanics, it is most common to assume an isotropic stress-strain relation, also due to the fact that model calibration can usually only operate with vertical land displacement information [30]. Stress-strain relationship is in

this theory expressed with Hook's law, which reads:

$$\begin{bmatrix} \sigma_{xx} \\ \sigma_{yy} \\ \sigma_{zz} \\ \tau_{xy} \\ \tau_{xz} \\ \tau_{yz} \end{bmatrix} = D \begin{bmatrix} \epsilon_{xx} \\ \epsilon_{yy} \\ \epsilon_{zz} \\ \epsilon_{xy} \\ \epsilon_{xz} \\ \epsilon_{yz} \end{bmatrix} \tag{2.8}$$

where σ_{ij} and τ_{ij} are the components of the effective stress tensor, and which can also be rewritten as $\boldsymbol{\sigma} = D\boldsymbol{\epsilon}$. The constitutive matrix for the isotropic and elastic medium (D) can be defined as:

$$D = \frac{E(1-\nu)}{(1+\nu)(1-2\nu)} \begin{bmatrix} 1 & \frac{\nu}{1-\nu} & \frac{\nu}{1-\nu} & 0 & 0 & 0 \\ \frac{\nu}{1-\nu} & 1 & \frac{\nu}{1-\nu} & 0 & 0 & 0 \\ \frac{\nu}{1-\nu} & \frac{\nu}{1-\nu} & 1 & 0 & 0 & 0 \\ 0 & 0 & 0 & \frac{1-2\nu}{2(1-\nu)} & 0 & 0 \\ 0 & 0 & 0 & 0 & \frac{1-2\nu}{2(1-\nu)} & 0 \\ 0 & 0 & 0 & 0 & 0 & \frac{1-2\nu}{2(1-\nu)} \end{bmatrix} \tag{2.9}$$

where E and ν are Young's Modulus and Poisson ratio respectively. These parameters are sufficient to describe the system's status and relate $\boldsymbol{\sigma}$ and $\boldsymbol{\epsilon}$. The relations between these values and the vertical uniaxial compressibility c_M can be expressed as follows:

$$c_M = \frac{(1+\nu)(1-2\nu)}{E(1-\nu)} \tag{2.10}$$

For a transversal isotropy model, where the elastic properties of a medium differ from the horizontal (expressed with h) to the vertical (expressed with z) plane, the constitutive matrix reads:

$$D = \begin{bmatrix} \frac{1}{E_h} & -\frac{\nu_h}{E_h} & -\frac{\nu_z}{E_z} & 0 & 0 & 0 \\ -\frac{\nu_h}{E_h} & \frac{1}{E_h} & -\frac{\nu_z}{E_z} & 0 & 0 & 0 \\ -\frac{\nu_z}{E_z} & -\frac{\nu_z}{E_z} & \frac{1}{E_z} & 0 & 0 & 0 \\ 0 & 0 & 0 & \frac{2(1+\nu_h)}{E_h} & 0 & 0 \\ 0 & 0 & 0 & 0 & \frac{1}{G_z} & 0 \\ 0 & 0 & 0 & 0 & 0 & \frac{1}{G_z} \end{bmatrix} \tag{2.11}$$

Finally, in a more general way, the compressibility reads:

$$c_M = \frac{1}{E_z}\left(1 - \frac{2\nu_z^2}{1-\nu_h}\frac{E_h}{E_z}\right) \tag{2.12}$$

It has been demonstrated by Gambolati et al. [1986] [14] that land displacement relies mostly on E_z. Both ν_z and ν_h have restricted variability, between 0 and 0.5 [17], thus playing a more limited role.

Finally, the relations between strains and displacement vector are:

$$\begin{aligned} \epsilon_{xx} &= \frac{\partial u}{\partial x} & \epsilon_{xy} &= \frac{1}{2}\left(\frac{\partial u}{\partial y} + \frac{\partial v}{\partial x}\right) \\ \epsilon_{yy} &= \frac{\partial v}{\partial y} & \epsilon_{yz} &= \frac{1}{2}\left(\frac{\partial v}{\partial z} + \frac{\partial w}{\partial y}\right) \\ \epsilon_{zz} &= \frac{\partial w}{\partial z} & \epsilon_{zx} &= \frac{1}{2}\left(\frac{\partial w}{\partial x} + \frac{\partial u}{\partial z}\right) \end{aligned} \tag{2.13}$$

2.3 Constitutive Laws

When describing the behavior of soil and, in particular, the stress-strain relation, the concept of constitutive laws has to be introduced.

Due to its simplicity, most applications use Hook's law to describe a linear elastic behavior under loading and unloading conditions, and Coulomb's law as failure criterion. Nonetheless, it is clear that these simple formulations cannot appropriately describe the domain response, as a time dependant and non-linear behavior has often been observed [32]. The discrepancies between pressure variation and land displacements must take into account the mechanical behavior of these deep formations, and should consider viscous effects [20]. The use of more accurate constitutive laws allows for a better analysis, as it is examined in the following chapter.

In the current project, the reservoir has been proven to be better described throughout a Soft Soil Creep Model (SSCM), which was first developed by Vermeer et al. in 1999 [33]. This model considers near-normally consolidated clay, clayey silts and peat as *soft soils* which possess a high rate of compressibility.

Strain rate is split into two components, plastic and elastic, and can be read as follows:

$$\dot{\boldsymbol{\epsilon}} = \dot{\boldsymbol{\epsilon}}^e + \dot{\boldsymbol{\epsilon}}^p \tag{2.14}$$

The elastic fraction can be further defined as:

$$\dot{\boldsymbol{\epsilon}}^e = D^{-1}\dot{\boldsymbol{\sigma}} \tag{2.15}$$

where $\dot{\boldsymbol{\sigma}}$ represents the rate of internal stress and D is once again the elastic matrix, function of ν and E.

This second parameter E is stress-dependent and is updated according to the following law, with k^* the modified swelling parameter:

$$E = -(1-2\nu)\frac{\sigma_{xx}+\sigma_{yy}+\sigma_{zz}}{k^*} \tag{2.16}$$

On the other hand, also plastic strain plays an important role and is governed by equation 2.17:

$$\dot{\boldsymbol{\epsilon}}^p = \dot{\gamma}\frac{\partial p_c}{\partial \boldsymbol{\sigma}} \tag{2.17}$$

where $\dot{\gamma}$ is the plastic multiplier rate and p_c is a representation of the stress state. In particular, p_c can be described as a plastic potential and denoted as:

$$p_c = p + \frac{c}{\tan\phi} + \frac{q^2}{M^2(p+\frac{c}{\tan\phi})} \tag{2.18}$$

In this equation:

- $p = -\frac{\sigma_{xx}+\sigma_{yy}+\sigma_{zz}}{3}$ is the volumetric stress;
- $q = \sqrt{\sigma_{xx}(\sigma_{xx}-\sigma_{yy})+\sigma_{yy}(\sigma_{yy}-\sigma_{zz})+\sigma_{zz}(\sigma_{zz}-\sigma_{xx})+3(\tau_{xy}^2+\tau_{yz}^2+\tau_{zx}^2)}$ is the deviatoric stress;
- c is the cohesion;
- ϕ is the friction angle;
- $M = 3\sqrt{\frac{(1-K_0^{NC})^2}{(1+2K_0^{NC})^2}+\frac{(1-K_0^{NC})(1-2\nu)\left(\frac{\lambda^*}{k^*}-1\right)}{(1+2K_0^{NC})(1-2\nu)\frac{\lambda^*}{k^*}-(1-K_0^{NC})(1+\nu)}}$, which corresponds to the slope of the Critical state line in the plane of the stress invariants.

The plastic multiplier rate present in 2.17 is instead defined as:

$$\dot{\gamma} = \frac{\mu^*}{\iota^*\frac{\partial p_c}{\partial p}}\left(\frac{p_c}{p_{c,r}}\right)^{\frac{\lambda^*-k^*}{\mu^*}} \tag{2.19}$$

where:

- ι^* is a time of reference which is related to normal-consolidation state when in a standard oedometer test;
- μ^* is the creep index;
- $p_{c,r}$ is the pressure obtained in a consolidation process at a reference strain rate $\frac{\mu^*}{\tau^*}$ and is referred to as preconsolidation equivalent pressure [20].

The ratio $\frac{p_c}{p_{c,r}}$ at the initial time, can be expressed as another parameter, called Overconsolidation Ratio (OCR):

$$\text{OCR} = \frac{\text{maximum effective stress ever experienced}}{\text{existing effective stress}} \tag{2.20}$$

A soil is said to be *overconsolidated* when the present effective stress has been exceeded in its stress history [9].

By following the approach developed by Vermeer, a three-dimensional Elasto-Plastic Rate Dependent Model (EPRDM) can be implemented into a Finite Elements (FE) geomechanical simulator, which will better discussed in the coming chapter.

The parameters required by SSCM are summarized here:

- c: cohesion [Pa];
- ϕ: friction angle;
- M: critical state line;
- ν: Poisson coefficient;
- λ^*: modified compression index;
- k^*: modified swelling index;
- μ^*: creep index;
- ι^*: reference time [s];
- $p_{c,r,0}$: initial reference stress [Pa].

It is useful to inquire and compare the effects of a rate-dependent and independent constitutive models in large scale conditions, since this can emphasize diverse behaviors from a mechanical viewpoint. Surface displacement can be affected and delayed, giving therefore a physical explanation for these conditions. A constant monitoring of the deformations can support in selecting the most suitable constitutive behavior by integrating point-scale provided information into averaged large scale values.

2.4 Faults and Fractures

When operating with the injection of fluids in an underground reservoir, it can happen to occur in related geomechanical issues. A common feature in deep reservoirs is the presence of faults. A geological fault is a discontinuity in a 3D porous medium and consists of two friction surfaces which are in contact with each other. The mechanical behavior of faults can be described through contact mechanics, and its fundamental aspects are traditionally traction balance, friction law on the fracture and nonpenetration condition.

Given these discontinuities within the subsurface, some further evaluations have to be discussed, with several consequences in effective stress changes within the domain.

In general, multiple issues can be associated with CO_2 sequestration from a geomechanical viewpoint:

1. The possible activation of sealing faults, which would lead to the creation of possible pathways for the CO_2 to escape.

2. Shear or tensile failure in the caprock and injected sandstone.

3. Ground deformation, which is of major concern for anthropogenic buildings or infrastructures, above or close to the reservoir [10, 6].

Generally, the strength acting on the fault can be divided into the normal and tangential component, $\mathbf{t} = \sigma_n \mathbf{n} + \boldsymbol{\tau}_s$ and, whenever normal stress is set as a negative value, this represents compression.

Particularly, faults activation can occur when shear stress acting on a failure plane exceeds a failure criterion. One of the most commonly accepted criteria to

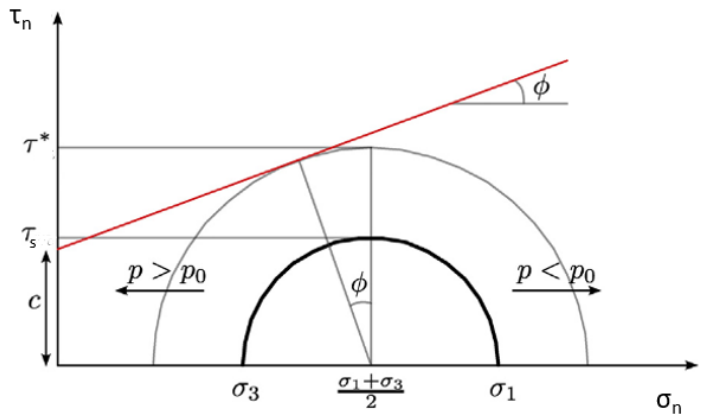

Figure 2.1: Representative stress state of a Porous medium expressed by Mohr's circle. Adapted from [31]

describe this behavior is the Coulomb criterion, that reads:

$$\|\boldsymbol{\tau}_s\| \leq c - \sigma_n \tan\phi \tag{2.21}$$

Where the shear and normal components of the stress acting on the fracture surface relate to the cohesion and the friction angle. Failure mechanisms can also have a graphical representation in Mohr's plane, as depicted in Fig. 2.1, where shear failure occurs whenever Mohr's circle touches the failure line. Moreover, tensile failure is described by the circle crossing the vertical axis.

Whenever this condition happens, the fault can slip, leading to a pathway for carbon dioxide escape, or even open in case of a normal tensile stress.

How close the fault is to being reactivated is analyzed by means of a *safety factor*, defined in [10]:

$$\chi = 1 - \frac{\tau_s}{\tau^*} \tag{2.22}$$

where $\tau_s = ||\boldsymbol{\tau}_s||_2$ and $\tau^* = c - \sigma_n \tan\phi$ are the actual shear stress and the maximum admissible shear stresses on the discontinuity surface, respectively. Whenever χ gets closer to zero, shear failure is likely to occur.

Gas injection is characterized by an increase in $\boldsymbol{\sigma}$, which can induce fault sliding and/or opening. Slippage is likely to happen in faults confining the site laterally and vertically, as the stiffness of the surrounding porous medium opposes the deformation of the reservoir. This can occur when the tangential component of the acting strength $\tau_s = \tau^*$, and its direction is expressed through

the now known shear vector $\boldsymbol{t}_t$ can be defined by [12] as:

$$\boldsymbol{t}_t = \tau^* \frac{\mathbf{u}_r}{\|\mathbf{u}_r\|} \tag{2.23}$$

with the subscript r meaning relative displacement. It reads:

$$\mathbf{u}_r = \mathbf{u}_b - \mathbf{u}_t \tag{2.24}$$

The normal contact conditions on the fracture can be summarized as:

- $\sigma_n = \mathbf{t} \cdot \mathbf{n} \leq 0$, defining that only compressive traction is allowed for;
- $g_n = \mathbf{u}_r \cdot \mathbf{n} \geq 0$, for non penetration condition;
- $\sigma_n g_n = 0$, stating that the fracture is either compressed or open.

While the conditions related to the frictional component are:

- $||\tau_s||_2 \leq \tau^*$, which is Coulomb's criterion;
- $\mathbf{g}_t \cdot \boldsymbol{t}_t - \tau^* ||\mathbf{g}_t||_2 = 0$, where frictional traction is aligned with sliding rate.

Where $\mathbf{u}_r = g_n \mathbf{n} + \mathbf{g}_t$ is the split of the relative displacement into normal and tangential components [13].

It is important to mention that the described geomechanical changes can occur not only in the area subjected to pressure variation, but also in overburden layers, as observed by [25]. Consequences can be noticed up to the surface above the site of interest, hence aspects such as ground deformation become also of vital importance, especially in on-shore applications. Ground ruptures have to be avoided as they can be the cause of CO_2 leakage and escape, but when dealing with off-shore sites, it is less probable that this behavior would damage the existing infrastructures.

To solve equation 2.5, a set of boundary conditions is required. They are Dirichlet and Neumann conditions:

- Dirichlet conditions define the displacement function on the boundary;
- Neumann conditions represent external loads.

3

Numerical Model

Once the appropriate mathematical model has been selected and proper boundary conditions have been set, a numerical approach can be used to approximate the solution. Since this problem is described throughout a system of partial differential equations (PDEs), the two most used numerical solution methods are:

- finite element (FE) method;
- finite volume (FV) method.

Both approaches discretize the domain of interest with a given set of elements/volumes. Based on this subdivision, a discrete version of the function space where the solution lies can be built using basis functions related to the discretization.

The present study focuses only on FE, traditionally more suited to solve structural problems. However, FV can be used as well. The presence of faults is incorporated into the model with the use of zero-thickness elements defined as Interface Elements (IE), which are fundamental for an appropriate description and modeling of the effects that these discontinuities cause in the domain. This is due to the fact that traditional finite elements do not allow relative movements between adjacent elements.

3.1 Weak form of the structural problem

The virtual work principle, needed to solve the governing equation with a variational method, reads:

$$\partial W_i - \partial W_e = 0 \tag{3.1}$$

where ∂W_i is the internal virtual work and ∂W_e the external. More specifically, in a 3D domain Ω, ∂W_i can be written also as:

$$\partial W_i = \int_\Omega \partial \boldsymbol{\epsilon}^T \boldsymbol{\sigma}\, dV \; - \int_\Omega \partial \boldsymbol{\epsilon}^T \mathbf{1} b p\, dV \tag{3.2}$$

since, according to Terzaghi's principle for porous media $\hat{\boldsymbol{\sigma}} = \boldsymbol{\sigma} - b\mathbf{1}p$.

The external work can be expressed as

$$\partial W_e = \int_\Omega \partial \mathbf{u}^T \rho_b \mathbf{g}\, dV \; + \int_{\partial\Omega} \partial \mathbf{u}^T \mathbf{t}\, dS \tag{3.3}$$

In a faulted reservoir, given the critical role played by the activation of faults, their contribution must also be considered in the formulation. By associating the virtual work equation in the continuum (3.1) to the current setting, it can be stated that:

$$\partial W_i + \partial W_f - \partial W_e = 0 \tag{3.4}$$

where the introduced term ∂W_f represents the fault virtual work. Considering a fault Γ in the 3D domain, it can be represented by a pair of inner surfaces, called Γ_t and Γ_b, where t and b stand for top and bottom respectively.

In this work, the contact constraints are imposed through the Lagrange multipliers technique. The strengths on the discontinuity surface, that coincide with the Lagrange multipliers $\boldsymbol{\lambda}$, ensure the continuity of displacement when the conditions expressed in 2.21 are verified. The fault portion where this criterion is not verified is defined as $\Lambda \subseteq \Gamma$. Describing the virtual work of the fault takes into consideration two attributes, one provided by virtual displacements and strengths where continuity of the solution is prescribed, and the other related to opening and sliding of the fault in its activated part. Equation 3.5 reads:

$$\partial W_f = \int_{\Gamma\setminus\Lambda} \partial \mathbf{u}_r^T \boldsymbol{\lambda}\, dS \; + \int_{\Gamma\setminus\Lambda} \partial \boldsymbol{\lambda} \mathbf{u}_r^T\, dS \; + \int_\Lambda \partial \mathbf{u}_r^T \mathbf{t}\, dS \tag{3.5}$$

Whenever opening occurs, the involved fault portion Λ does not contribute to

virtual work, since both normal and shear strength are null ($\lambda_n = \boldsymbol{\lambda}_s = 0$). Equation 3.4 can be explicitly rewritten as:

$$\int_\Omega \partial\boldsymbol{\epsilon}^T \boldsymbol{\sigma}\, dV + \int_{\Gamma\setminus\Lambda} \partial\mathbf{u}_r^T \boldsymbol{\lambda}\, dS + \int_{\Gamma\setminus\Lambda} \partial\boldsymbol{\lambda}^T \mathbf{u}_r\, dS + \int_\Lambda \partial\mathbf{u}_r^T \mathbf{t}\, dS = \int_\Omega \partial\boldsymbol{\epsilon}^T \mathbf{1} bp\, dV + \int_\Omega \partial\mathbf{u}^T \rho_b \mathbf{g}\, dV + \int_{\partial\Omega} \partial\mathbf{u}^T \mathbf{t}\, dS \tag{3.6}$$

By using an uncoupled approach, in this work the pore pressure p is an external source of strength, which is provided by a flow model.

3.2 Finite Element Method

This section presents the FE method firstly by providing its general formulation, and afterwards with the detailed specific case used in the current thesis.

3.2.1 General formulation

By solving the numerical model, the displacement can be approximated at the point $\mathbf{x}$ by the function $\mathbf{u}^h(\mathbf{x}) \in \mathcal{U}^h$, with $\mathcal{U}^h$ a finite Hilbert function space, which is generated by piecewise polynomials corresponding to the FE nodes in the domain. In a compacted form this expression can be written as:

$$\mathbf{u}^h(\mathbf{x}) = N_u(\mathbf{x})\mathbf{u} \tag{3.7}$$

with $N_u(\mathbf{x})$ a matrix collecting trilinear basis functions, selected in accordance to the use of hexahedral elements to discretize the domain. The vector $\mathbf{u} = [u, v, w]^T$ represents the nodal displacement in a 3D setting.

Likewise:

$$\boldsymbol{\lambda}^h(\mathbf{x}) = N_\lambda(\mathbf{x}) R \boldsymbol{\lambda} = N_\lambda(\mathbf{x}) \boldsymbol{\lambda}_g \tag{3.8}$$

with the fault strength approximated by $\boldsymbol{\lambda}^h(\mathbf{x}) \in \mathcal{L}^h$, which again is a finite Hilbert function space generated by piecewise polynomials corresponding to the FE nodes in $\Gamma^t \equiv \Gamma^b$. The subscript g refers to the global nodal strength, related to the local strength by the rotation matrix R.

Matrices S^t and S^b map the nodal displacements on the fault surfaces from

$\mathbf{u}$ and can be used to rewrite the relative displacement as:

$$\mathbf{u}_r^h = N_u S^b \mathbf{u} - N_u S^t \mathbf{u} = N_u S \mathbf{u} \tag{3.9}$$

Under the hypothesis of small deformations, strains as reported in 2.13 can be approximated as:

$$\boldsymbol{\epsilon}^h = L\mathbf{u}^h = LN_u\mathbf{u} = B\mathbf{u} \tag{3.10}$$

where L is the first order differential operator that relates strain to displacement, and B the deformation matrix.

The effective stress, according to the constitutive model that is selected, can be written as:

$$d\boldsymbol{\sigma}^h = D_t \, d\boldsymbol{\epsilon}^{\boldsymbol{h}} \tag{3.11}$$

with D_t tangent constitutive matrix.

The discrete shear strength $\boldsymbol{\tau}^{*h}$ along Λ is related to $\mathbf{u}_r^h$ according to equation 2.23, also referred to as *principle of maximum plastic dissipation*. By using the defined function $\boldsymbol{\lambda}^h$ and with $\mathbf{n}$ the vector normal to Λ, τ^* is:

$$\tau^* = c - \tan\varphi \mathbf{n}^T N_\lambda R\boldsymbol{\lambda} \tag{3.12}$$

Introducing the term $\|\mathbf{u}\|_H = \sqrt{\mathbf{u}^T H \mathbf{u}}$ as the H-energy norm of $\mathbf{u}$, with $H = S^T N_u^T N_u S$, positive and semi-definite matrix, vector $\boldsymbol{\tau}^{*h}$ can be written as:

$$\boldsymbol{\tau}^{*h} = (c - \tan\varphi \mathbf{n}^T N_\lambda R\boldsymbol{\lambda}) \frac{N_u S\mathbf{u}}{\sqrt{\mathbf{u}^T S^T N_u^T N_u S \mathbf{u}}} = (c - \tan\varphi \mathbf{n}^T N_\lambda R\boldsymbol{\lambda}) \frac{N_u S\mathbf{u}}{\|\mathbf{u}\|_H} \tag{3.13}$$

The final numerical model can therefore be described by adding these expressions inside equation 3.6, which represented the general virtual work principle, and read:

$$\begin{aligned} &\partial\mathbf{u}^T \int_\Omega B^T \boldsymbol{\sigma}^h \, dV \; + \partial\mathbf{u}^T \int_{\Gamma\setminus\Lambda} S^T N_u^T N_\lambda R\boldsymbol{\lambda} \, dS \; + \partial\boldsymbol{\lambda}^T \int_{\Gamma\setminus\Lambda} R^T N_\lambda^T N_u S\mathbf{u} \, dS \; + \\ &+ \partial\mathbf{u}^T \int_\Lambda (c - \tan\varphi \mathbf{n}^T N_\lambda R\boldsymbol{\lambda}) \frac{H\mathbf{u}}{\|\mathbf{u}\|_H} \, dS \; = \\ &= \partial\mathbf{u}^T \int_\Omega B^T \mathbf{1} bp \, dV \; + \partial\mathbf{u}^T \int_\Omega N_u^T \rho_b \mathbf{g} \, dV \; + \partial\mathbf{u}^T \int_{\partial\Omega} N_u^T \mathbf{t} \, dS \end{aligned} \tag{3.14}$$

This equation has to be true for any virtual displacement $\partial\mathbf{u}$ and virtual

strength $\partial\boldsymbol{\lambda}$. This can be rearranged as a non-linear system with unknown $\mathbf{u}$ and $\boldsymbol{\lambda}$, in a compacted form as:

$$\begin{cases} F_1(\mathbf{u}, \boldsymbol{\lambda}) = 0 \\ F_2(\mathbf{u}, \boldsymbol{\lambda}) = 0 \end{cases} \tag{3.15}$$

where F_1 solves the approximated final numerical model, and F_2 expresses the non-respect of constrains, such as non penetration. The resolution of the system 3.15 is carried out with the Newton scheme that, starting from an initial value, proceeds as in 3.16. The solutions are computed by solving the linear system with the Jacobian matrix $J^{(k)} = J(\mathbf{u}^{(k)}, \boldsymbol{\lambda}^{(k)})$:

$$\begin{bmatrix} \mathbf{u}^{(k+1)} \\ \boldsymbol{\lambda}^{(k+1)} \end{bmatrix} = \begin{bmatrix} \mathbf{u}^{(k)} \\ \boldsymbol{\lambda}^{(k)} \end{bmatrix} + \begin{bmatrix} \delta\mathbf{u} \\ \delta\boldsymbol{\lambda} \end{bmatrix} \quad \text{and} \quad J^{(k)} \begin{bmatrix} \delta\mathbf{u} \\ \delta\boldsymbol{\lambda} \end{bmatrix} = - \begin{bmatrix} F_1 \\ F_2 \end{bmatrix} \tag{3.16}$$

In this way, convergence is achieved when a vector norm, that can be either the norm of the displacement increment or the norm of unbalanced forces, usually normalized by its initial value, gets below a previously defined tolerance [12].

Finally, further details can be useful to fully define the numerical modeling of faults. As already mentioned, they are incorporated into the 3D model and substantially improve the prediction of both stress and displacement. The most common method used to simulate the mechanics of faults is based on zero-thickness elements which can describe behavior such as slippage or openings, and which are usually referenced as IE. This formulation is one of the many that have been based on the studies conducted by Goodman et al. in 1968 [18].

It can be said that the main feature characterizing IE formulations have been reviewed in literature and mainly depend on aspects such as:

- the chosen disctretized unknowns, which can be stress, displacement or both;
- the exact imposition of a constitutive law for contact, such as Coulomb or Tresca among others;
- the algorithm used to solve contact constrains, such as the penalty method or, as in this case, Lagrange multipliers.

Moreover, as described in [12], the activation of the fault is the main non-linearity of the model, and operating modes from a numerical point of view can be set as:

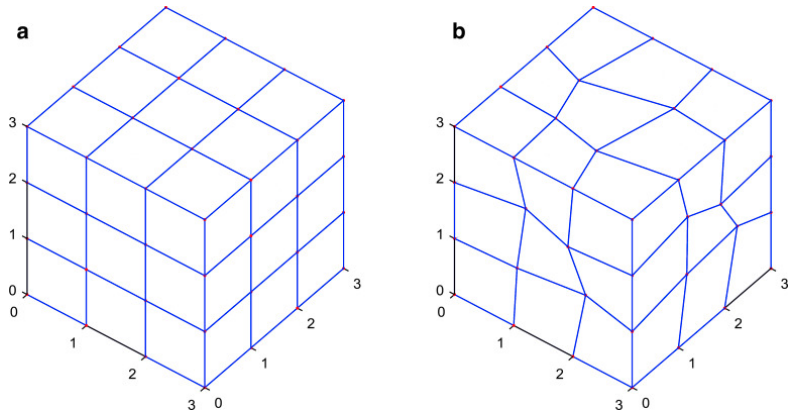

Figure 3.1: Hexahedral Finite elements grid examples, with regular (a) and irregular (b) elements. Adapted from [22].

- Full opening: the nodes are not in contact and a free relative displacement is allowed. The Lagrange multipliers are known and equal to zero;
- Full closure: the fault is compressed and the Coulomb criterion is satisfied. The Lagrange multipliers are unknown and no relative movement is allowed for between two corresponding nodes;
- Slipping: the fault is compressed, but the limit shear strength is not able to prevent sliding. The Lagrange multiplier λ acting on the normal direction is unknown, while the components lying on the contact surface are computed using equation 2.23.

3.2.2 Specific case

In this study, the mechanical equilibrium equation is solved using the GEPS3D code, a finite element simulator developed by the University of Padova [10, 30]. The finite elements which were selected to describe the site are eight-node hexahedral elements (Fig. 3.1), which demonstrate to be less influenced by the degree of refinement of the grid, when compared to the thetrahedral elements. For a generic finite element e, the shape function P_i^e, which is used to interpolate the variable within elements, and is associated to the nodes $i = 1, .., 8$ of the elements, is:

$$P_i^e = \frac{1}{8}(1-\xi)(1-\eta)(1-\zeta) \tag{3.17}$$

expressed in the local reference frame (ξ, η, ζ). By multiplying the shape function by the identity matrix $P_i^e I_8 = N_u^e$, with obtained N_u^e known as basis function.

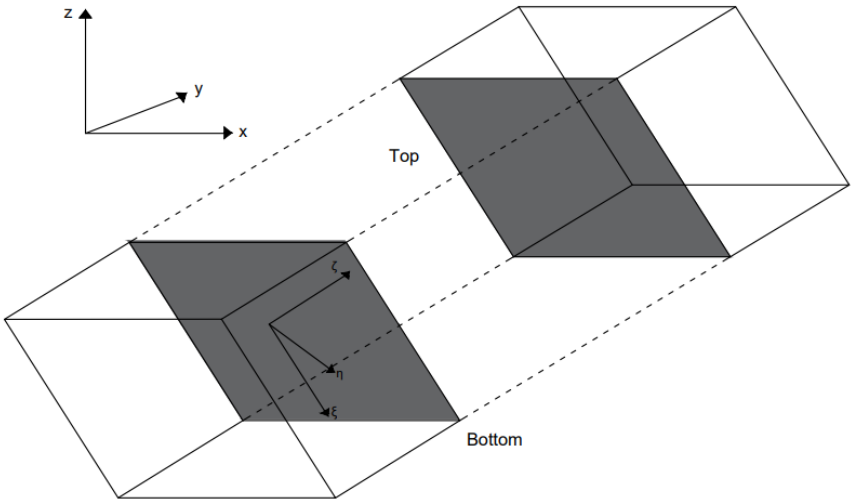

Figure 3.2: Linear IE connected to a 3D mesh.

In the same way, N_λ^e quoted in equation 3.8 can be expressed as $N_\lambda^e = \theta_i^e I_4$, where $\theta(\mathbf{x})$ is a piecewise constant function, with $\theta(\mathbf{x}) = 1$ if the point $\mathbf{x}$ is inside the area associated with a considered node.

Regarding the constitutive law, a correct description depends much on aspects like process scale and, as it happens in this study, Coulomb strength criterion is favoured at a macroscale level [11].

An example of zero-thickness IE which corresponds to the specific case is depicted in Fig. 3.2, where the pair of bilinear elements with coinciding nodes can be observed. It must be noted that the considered case has quadrilateral IE, in accordance with the hexahedral mesh (the specific mesh used in this thesis can be found in Chapter 4, Figure 4.1). Moreover, the local reference frame helps in identifying the normal and transversal direction of the element.

For a more comprehensive discussion on the topic, the reader can consult the work by Franceschini et al. [12], which provides additional insights.

4

Site Description

The site investigated in the current thesis work is located in the offshore of the Adriatic Sea, northern Italy. A geomechanical simulation is performed in a geological formation where a potential injection of CO_2 could occur, with the objective of analyzing the related surface displacements and possibly investigating the potential activation of sealing faults located in the surroundings of a depleted hydrocarbon reservoir.

The reservoir is located between 1500 and 3800 m below the mean sea level and has been developed since the late '60s. From a sedimentological and structural point of view, the site has turbiditic origins, from Marine Quaternary to Pliocene, and results from extensive tectonic activity during the Jurassic and Cretaceous period with compressive activity until the present day.

Fig. 4.1 shows grid developed to discretize the model domain. It covers an area of 57x31 km^2, with a depth range down to 8 km. The 3D mesh consists of 1,274,490 hexahedral elements and 62,242 quadrilateral interface elements, and a total of 1,376,846 nodes. The mesh is more refined, in both vertical and horizontal directions, near the reservoir. This is due to the need for a more accurate description in that location, and also by the morphology of the reservoir itself.

Five different layers associated with different materials' properties are modeled:

- Overburden, with an elevation between -13 m and -1460 m;
- Sideburden, with an elevation between -1460 m and -5100 m;

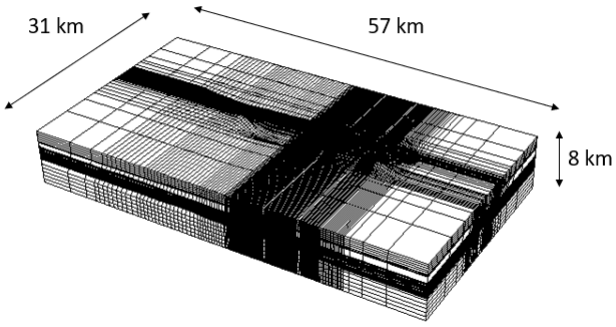

Figure 4.1: 3D mesh of the investigated site. The mesh consists of 1,274,490 hexahedral elements and 62,242 quadrilateral interface elements, with a total of 1,376,846 nodes.

- Interlayer, with an elevation between -1460 m and -5100 m;
- Reservoir, with an elevation between -1460 m and -4700 m, but intertwined with the interlayers;
- Underburden, with an elevation between -5100 m and -8000 m.

The various layers are represented in an axonometric projection of the mesh in Fig. 4.2, where the level of detail and variability for the elements along the vertical axis are well represented. They can also be observed along section A-A' in Fig. 4.3, where the five top layers are colored in blue, the five bottom layers in light blue, reservoir and interlayer are red and yellow respectively, and the sideburden is in green.

The reservoir is surrounded by eleven sealing faults which act as impermeable boundaries for the propagation of CO_2 and pore pressure, while could potentially jeopardize the results of the sequestration process if reactivated by the change of the natural stress regime. The system of faults is depicted in Fig. 4.5. A top view can be observed in Fig.4.4.

A more detailed stratigraphy of the site can be observed in Fig. 4.6, where the depth interval of reservoir involved in the extraction and then selected for the CCS development is here depicted in purple and indicated as TOP-PL2C. The depth range is comprised between approx -2800 and -3000 m below sea level. Another aspect that this section highlights is the layering offset along a few sealing faults bounding the reservoir, and denoted as fault 11 (also referred

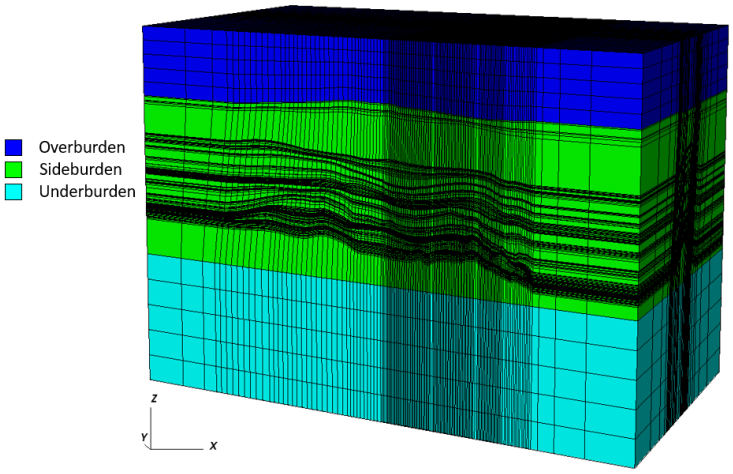

Figure 4.2: Axonometric view of the 3D domain. The vertical scale is exaggerated by a factor 5 with respect to the horizontal scale.

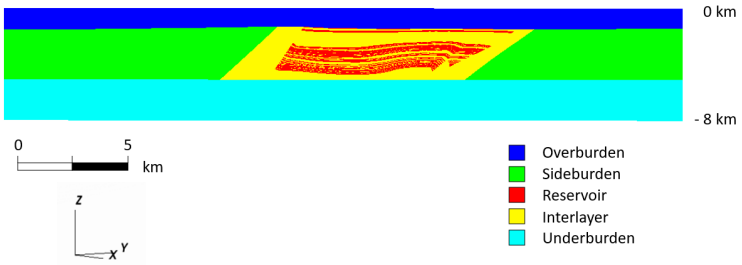

Figure 4.3: Model domain along section A-A′ (as in Fig. 4.4) with a detail on the 5 materials composing the 3D mesh. The reservoir and interlayer are in red and yellow respectively.

to as fault-south), fault 3, and fault 1. The discontinuity in the domain that these fractures cause is well expressed in this figure.

The primary production phase began in 1969 and lasted until the early 2000s. This is clearly visible by the time trend of the normalized pressure in the reservoir as shown in Fig. 4.7. The pressure recovery observed after the end of production, which is due to natural groundwater flow from the aquifer surrounding the reservoir, made the site perfect for a first attempt to inject CO_2. Pressures are normalized relative to the initial pressure value before the beginning of production due to confidentiality reasons.

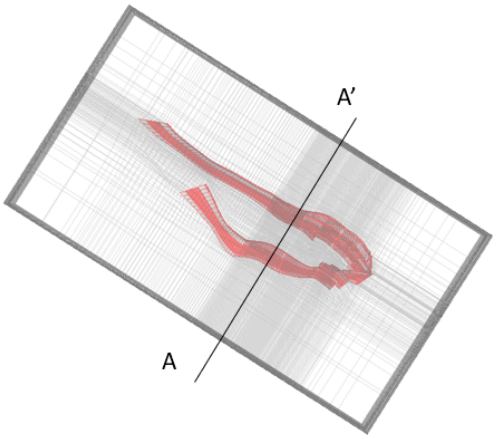

Figure 4.4: Top view of the fault system within the domain. Section A-A′ is highlighted.

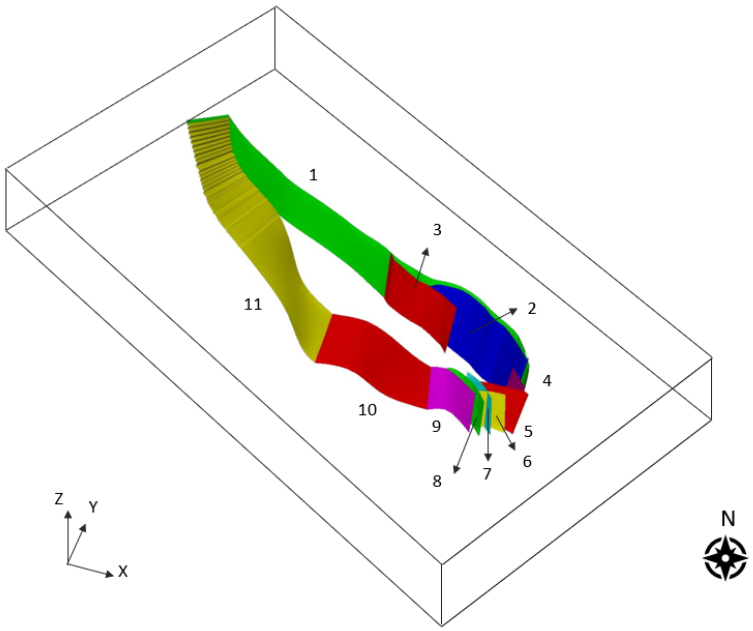

Figure 4.5: Axonometric projection of the fault planes with reference number.

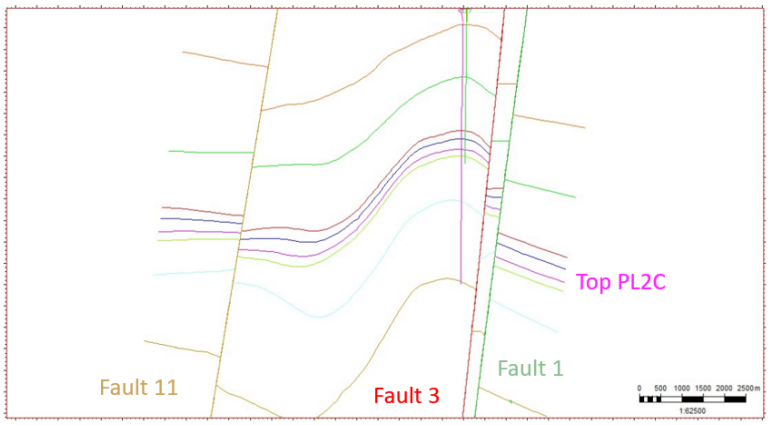

Figure 4.6: Traces of the production and injection wells projected along the vertical section A-A'.

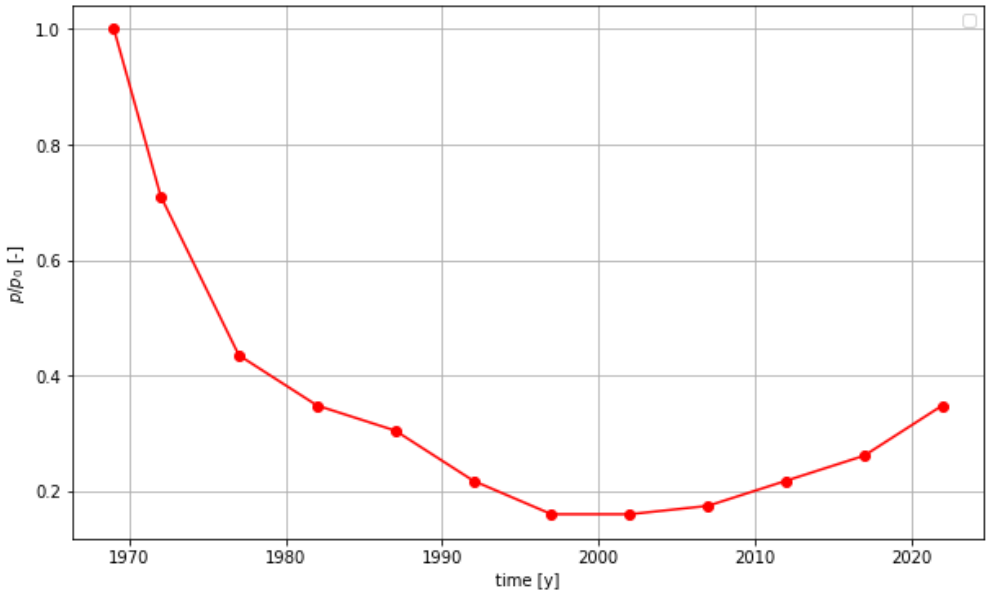

Figure 4.7: Behavior versus time [years] of the normalized pressure in the reservoir over the production phase.

5

Numerical Simulations

This chapter reports the settings and results of the performed numerical simulations, which can be divided into two main sections:

- Section 5.1: Primary production from the unit PL2C of the reservoir;
- Section 5.2: CCS simulation, with CO_2 injection performed in a portion of the unit PL2C.

The model has been preliminary run to check for consistency characterizing the entire domain with a linear elastic behavior. Parameters from previous studies, such as the one carried out by Castelletto et al. [5] or Teatini et al. [29] in the area, and data provided by the production company are used (Table 5.1).

E_z [MPa]	3.217
ν_z	0.3
E_h/E_z	1.0
ν_h/ν_z	1.0

Table 5.1: Input parameters for the simulations using a linear elastic law.

The description of the mechanical behavior of the reservoir and interlayers has then been improved using SSCM relationship. The set of parameters representative of the SSCM behavior for the site of interest are provided by the energy company and are listed in Table 5.2. A parametric analysis has been performed

for both sets of simulations to analyze the model sensitivity, in terms of displacement, to changes in viscosity or elastic /plastic compressibility parameters.

c [MPa]	0
ϕ	30
M	1.330
ν_v	0.3
E_h/E_z	1.0
ν_h/ν_z	1.0
λ^*	4.630×10^{-2}
k^*	6.290×10^{-3}
μ^*	8.378×10^{-4}
ι^* [s]	2.700×10^{-3}
OCR	1.379

Table 5.2: Original input parameters for the simulations using SSCM. Refer to Section 2.3 for parameter explanation.

For both simulations, the parametric analyses have been based on the following four scenarios:

- S1: The whole domain is characterized by a linear elastic relationship;
- S2: SSCM is assigned to reservoir and the interlayers, with the original parameters provided by the energy company given in Table 5.2;
- S3: as S2 with $\mu*$ decreased by one order of magnitude, from 8.370×10^{-4} to 8.370×10^{-5};
- S4: as S2 with OCR increased from 1.379 to 2.379.

Notice that in the following the suffix (P) is used to indicate primary production and (I) to indicate CO_2 injection.

The change in stress field has been also investigated for all the simulated cases. It is important to mention that, among the valuable information provided by the energy company, the behavior of the vertical effective stress with z (Fig. 5.1) has been supplied, allowing for more realistic analyses.

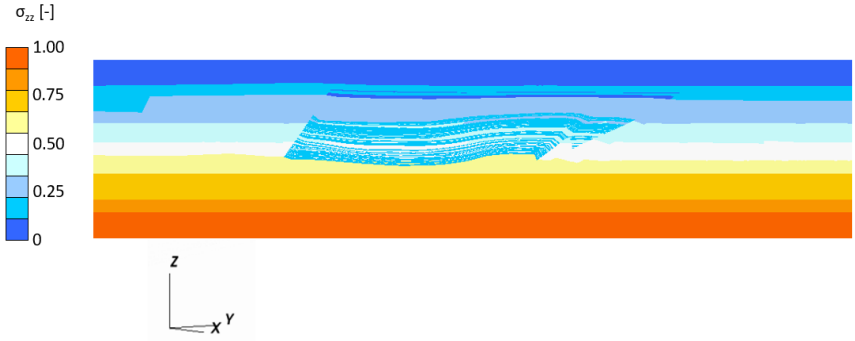

Figure 5.1: Section A-A' with initial distribution of σ_{zz} normalized over the largest value.

5.1 Primary production

5.1.1 Model Set-up

The primary production from the reservoir, which has already been introduced in Chapter 4, has been simulated by the geomechanical model to characterize the stress field at the inception of the CO_2 injection and perform a sensitivity analysis of the displacement field in the surroundings of the extraction/injection area. The simulations cover a time frame of 53 years, starting from 1969 until the present day, here set as the year 2022. The pressure variation experienced by the reservoir is provided in the previous chapter (Fig. 4.7).

The reservoir portion affected by pressure variation has been chosen based on the available information. Most likely, it does not cover the entire volume affected by the depletion during the production stage. A detailed top view picture of the area in which the pressure variation has been considered to develop is provided in Fig. 5.2.

5.1.2 Result discussion

The parametric analysis carried out for the primary production phase has allowed to highlight interesting aspects of the model response in relation to the variability of the constitutive laws. The simulation results are provided in terms of displacement along the vertical and horizontal directions of the land surface. As expected, a downward movement of the land surface has been obtained in all simulations, expressed by the positive values of the normalized vertical displacement w. Table 5.3 summarizes the numerical results of the simulations,

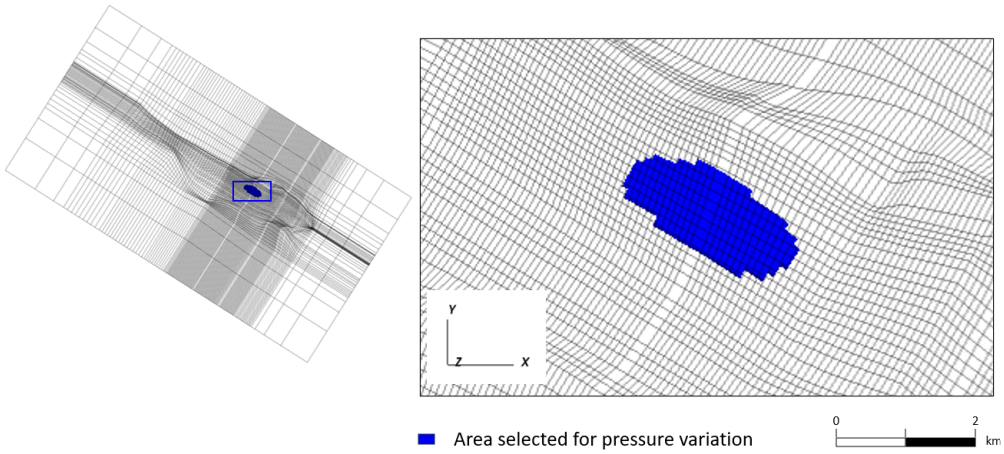

Figure 5.2: Top view close-up of the area involved by the primary production in terms of pressure variation.

presenting the maximum vertical displacement for the two most significant time frames corresponding to the end of production phase (1997) and the present day (2022). The behavior versus time of the same quantity is shown in Fig. 5.3. The values have been normalized to respect to the largest (vertical) displacement (subsidence), which was obtained with the S2-P simulation at the present day.

An in-depth analysis of the results obtained with the various scenarios is provided in the following subsections. Notice that the various maps and sections produced to show the pattern of the normalized vertical displacements are bounded between ±0.4 to better capture the domain portion experiencing the movements. Concerning the normalized horizontal displacements u and v, which have been normalized again with respect to the largest vertical displacement computed in the scenario S2-P at 2022, the visualization scale has been limited by ±0.3, since u and v are smaller than w.

Additionally, some final considerations are drawn based on the development of the stress fields in the different cases. The stresses are normalized by the maximum initial value of vertical effective stress, at the bottom of the domain. A visualization scale ranges between ±0.16, corresponding to the largest variation.

S1-P: Linear elastic

The elastic parameters used to characterize the first scenario (S1-P) yield a quite stiff soil, allowing for relative small displacement. In fact, the computed downward movement is almost one order of magnitude smaller than the one

TIME [y]	1997	2022
S1-P	0.1803	0.1399
S2-P	0.9174	1
S3-P	0.5906	0.5883
S4-P	0.1107	0.1013

Table 5.3: Largest normalized vertical displacement w of the land surface during primary production at two significant times.

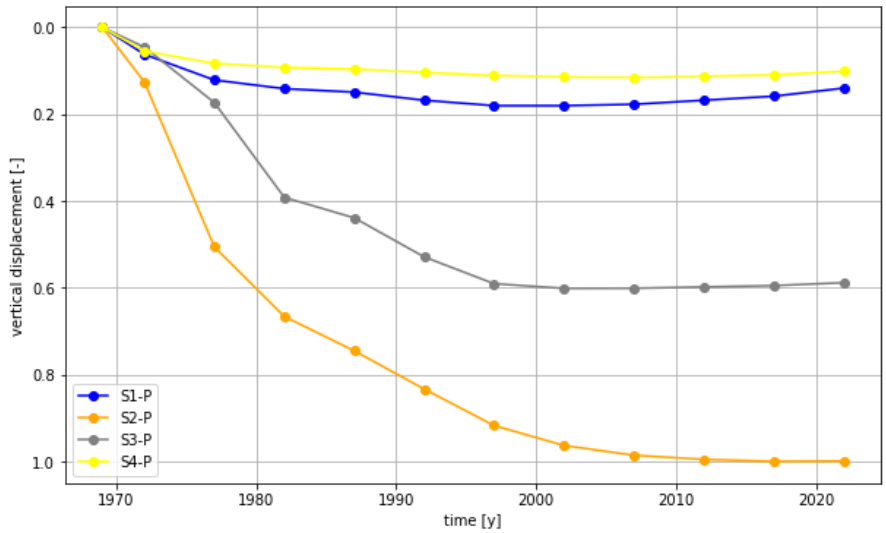

Figure 5.3: Behavior versus time of the normalized vertical displacement w during primary production.

computed in scenario S2-P (Fig. 5.3).

The largest value in terms of w for this simulation is obtained at the end of the production phase. The behavior of the curve in Fig. 5.3 depicts a displacement evolution that reflects the one of the pressure, with the end of subsidence coinciding with the end of the actual production phase, between 1997 and 2002, and a certain rebound afterwards as clearly detectable by comparing Fig. 5.4 and 5.5. Fig. 5.6 shows the w distribution along the vertical section A-A'. It must be noted that the negative value below the reservoir means that the portion of the domain moves upward due to the reservoir compaction. The pattern of the horizontal displacements u and v are depicted in Fig. 5.7 and 5.8, respectively. As expected, they are characterized by smaller values relative to the vertical component.

The change in stress field is another important result of the model, especially when faults cross or bound the reservoir. Fig. 5.9 presents a vertical section with the variation of normal stress along the z axis. Here the displayed results are normalized, and an increase of the vertical effective stress is represented by the positive sign. Propagation of the stress is very limited, and coherent with pressure variation: the effective stress increases in the reservoir layer (greenish colors) and gently decreases above and below (pink colors). The variation of σ_{zz} is about three times larger than the horizontal components, which are not provided given their limited variation. The extension of the variation resembles the area where the pressure change is imposed, and no significant propagation occurs outside this area.

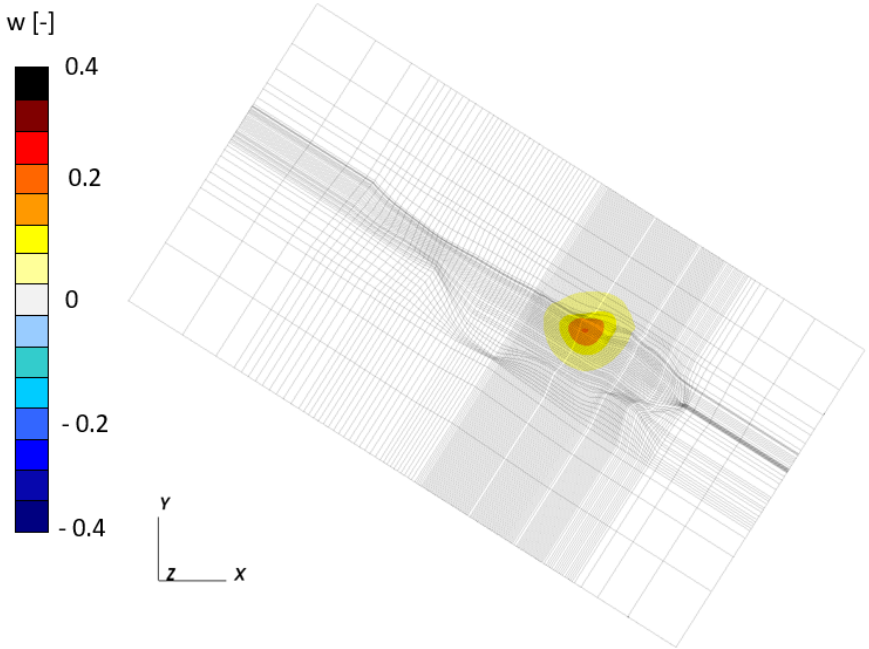

Figure 5.4: Normalized vertical displacement w with scenario S1-P at the end of the production phase in 1997.

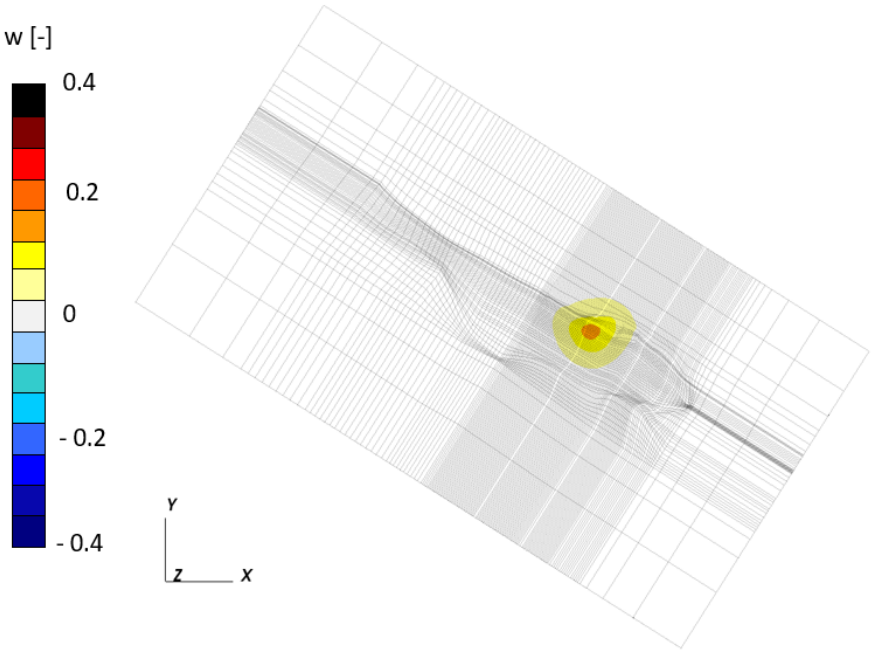

Figure 5.5: Normalized vertical displacement w with scenario S1-P in 2022.

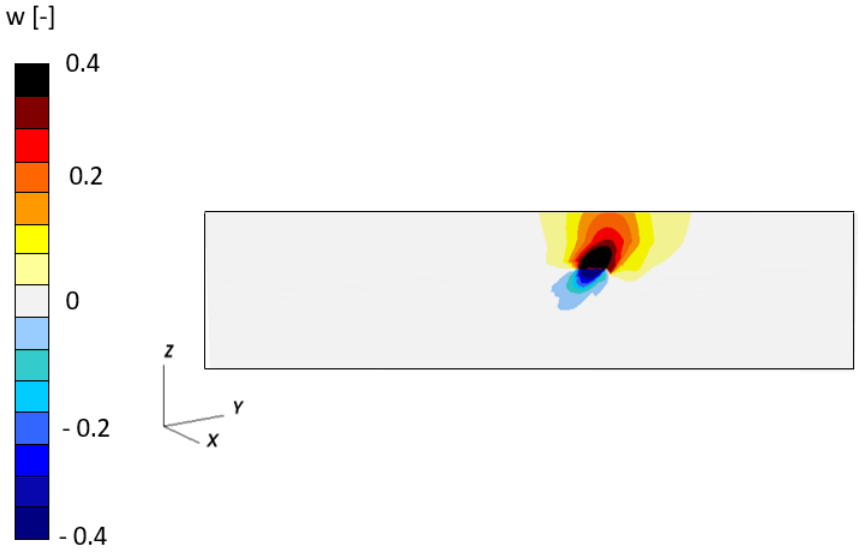

Figure 5.6: Normalized vertical displacement w along section A-A′ with scenario S1-P at the end of the production phase in 1997.

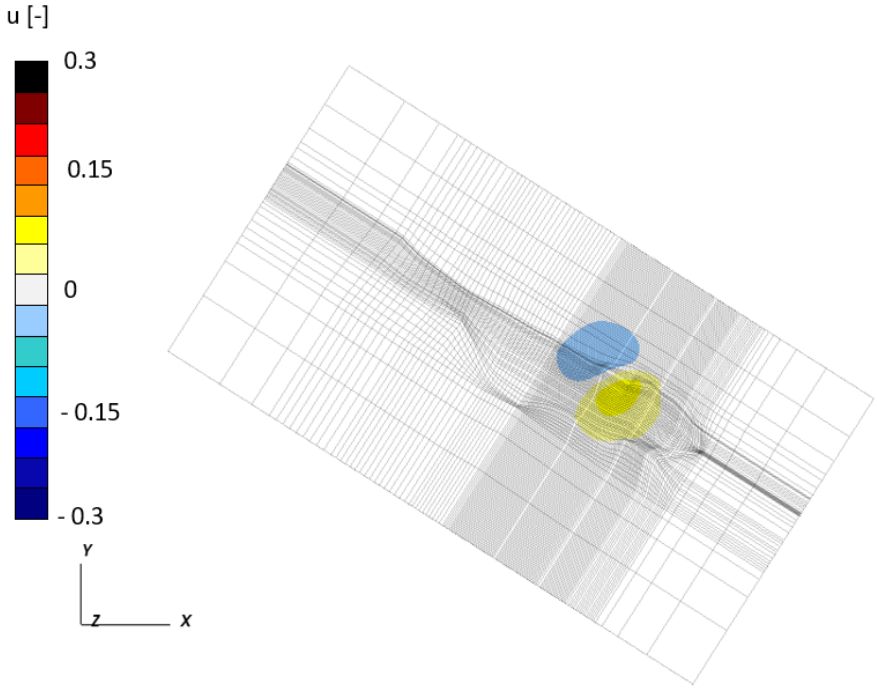

Figure 5.7: Normalized horizontal displacement u with scenario S1-P at the end of the production phase in 1997.

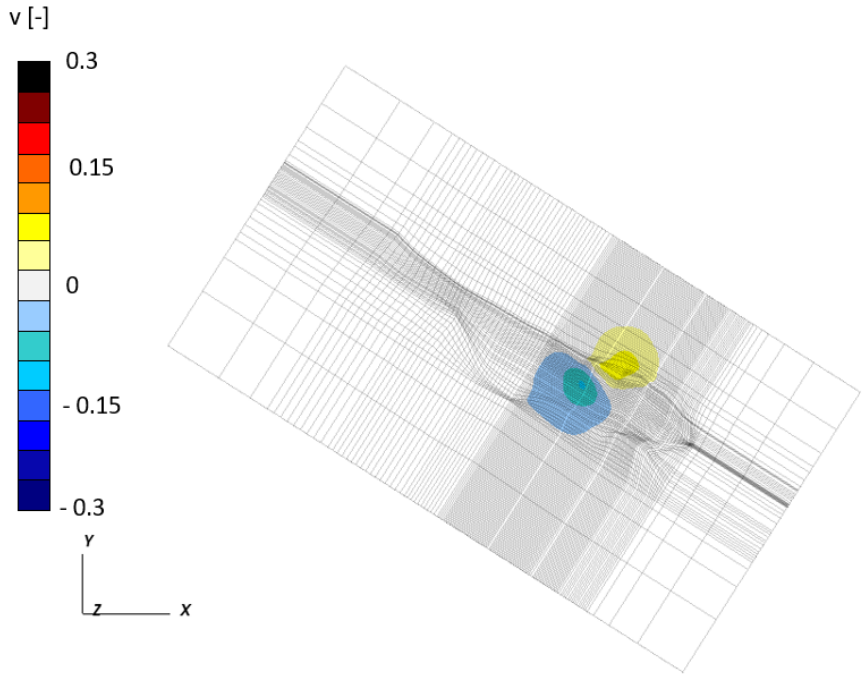

Figure 5.8: Normalized horizontal displacement v with scenario S1-P at the end of the production phase in 1997.

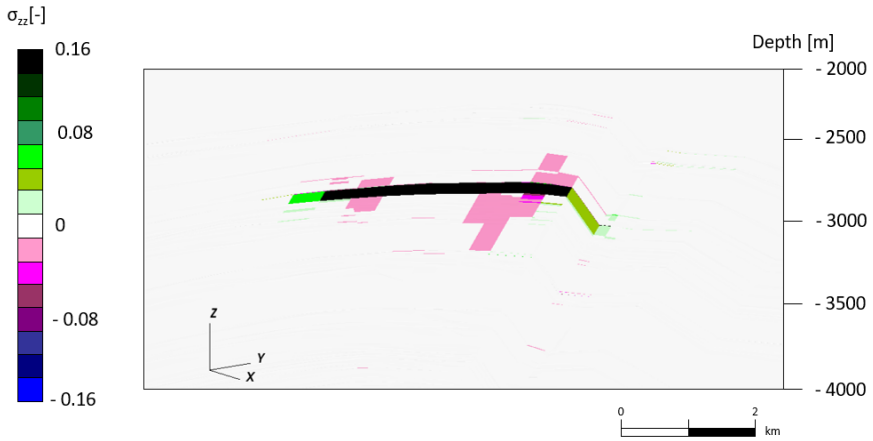

Figure 5.9: Variation of σ_{zz} between initial condition and end of the production phase in 1997 with scenario S1-P along a portion of section A-A′.

S2-P: SSCM

The peculiarity of the results obtained using the SSCM constitutive model with the "original" parameter values provided by the energy company is the delayed subsidence that continues even after the end of the production phase. This behavior is strictly related to viscous deformations. Moreover, the displacements caused by the reservoir development result much larger in this scenario than in the previous one.

Figs. 5.4 and 5.5 show w in 1997 and 2022. In this scenario the subsidence caused by the extraction is not limited to an area above the extraction well, but expands through a larger portion of the domain, reaching the extremities of the reservoir material in 2022. Moreover, Fig. 5.12 brings the attention to the increased area where land movement occurs, and offers a good comparison with the vertical section of case S1-P in Fig. 5.23. These features highlight a possibly too large viscous deformation, a part of which is caused by the load of the soil itself. Most likely, the original value of μ^* is too large and improper to describe the domain behavior during the production phase.

The horizontal displacements are shown in Figs. 5.13 and 5.14 at the present day in 2022, where the largest values can be observed accordingly to vertical displacement. Also in this scenario the horizontal components of the movement are smaller than the vertical one.

Although the current study presents several limitations, for example due to the fact that no real information is available concerning the actual volume experiencing the pressure decline caused by the gas withdrawal, nevertheless the w trend obtained with the S2-P scenario is supported by existing literature. Palano et al. [24] published a collection of displacement records measured by Global Navigation Satellite Systems (GNSS) antennas established on offshore platforms in the Adriatic Sea. In relation to the reservoir of interest, the values measured by GNSS starting from 2003 are in agreement with the trend provided by S2-P simulation.

Regarding the variation of σ_{zz}, the distribution along a vertical section of the results obtained for S2-P is provided in Fig. 5.15. The changes are larger than those computed with the scenario S1-P, and also the volume experiencing the stress change is larger than in the previous case, although it does not propagate far from the reservoir unit.

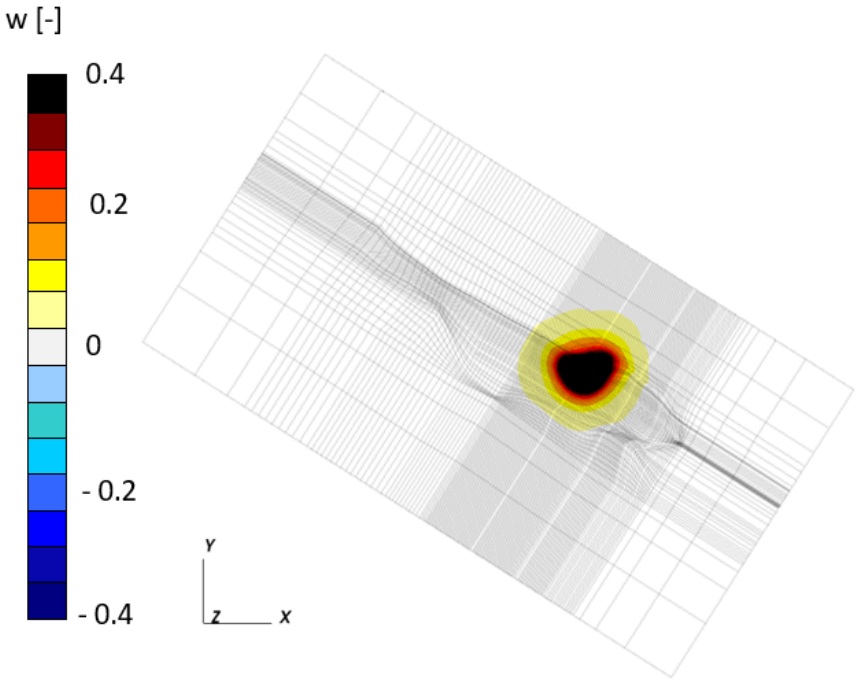

Figure 5.10: Normalized vertical displacement w with scenario S2-P at the end of the production phase in 1997.

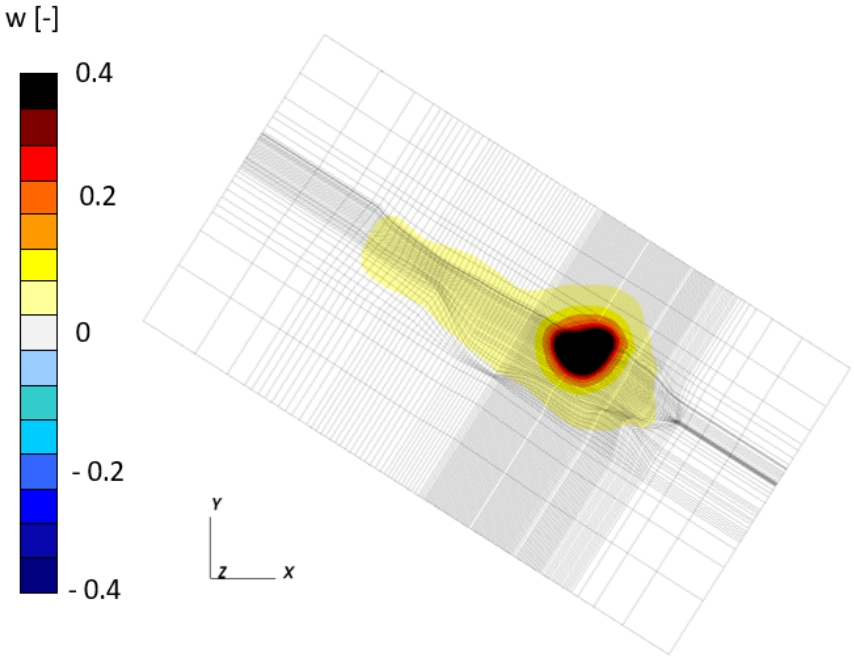

Figure 5.11: Normalized vertical displacement w with scenario S2-P in 2022.

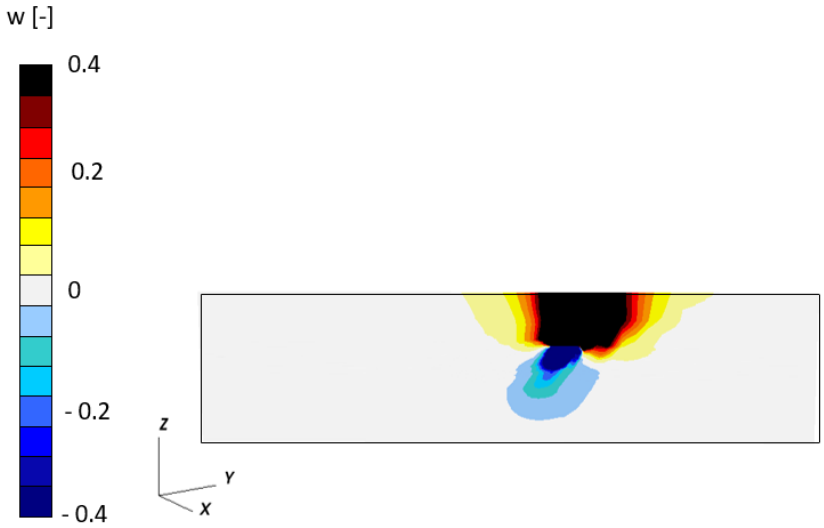

Figure 5.12: Normalized vertical displacement w along section A-A' with scenario S2-P at the end of the production phase in 1997.

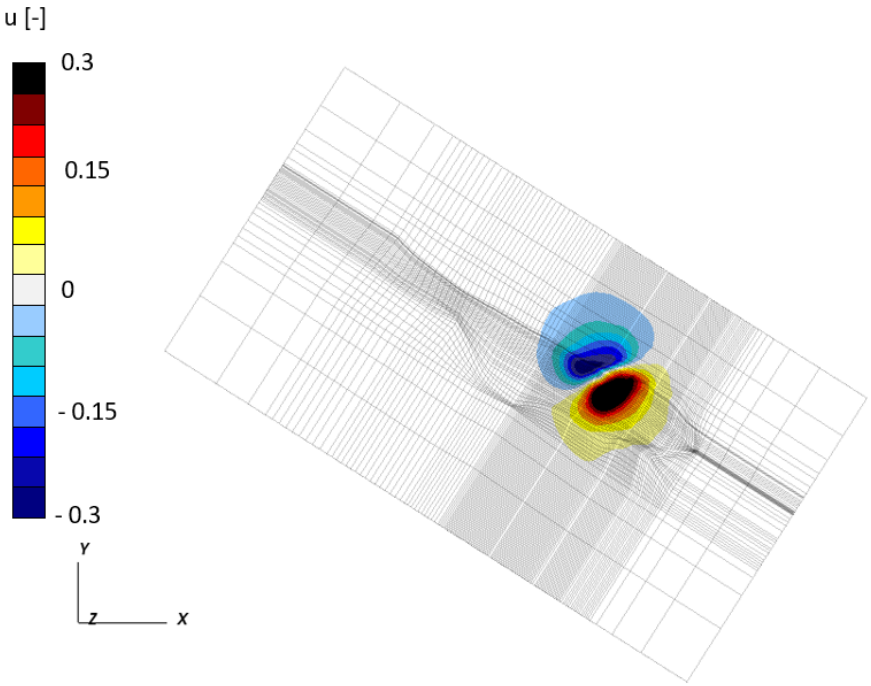

Figure 5.13: Normalized horizontal displacement u with scenario S2-P in 2022.

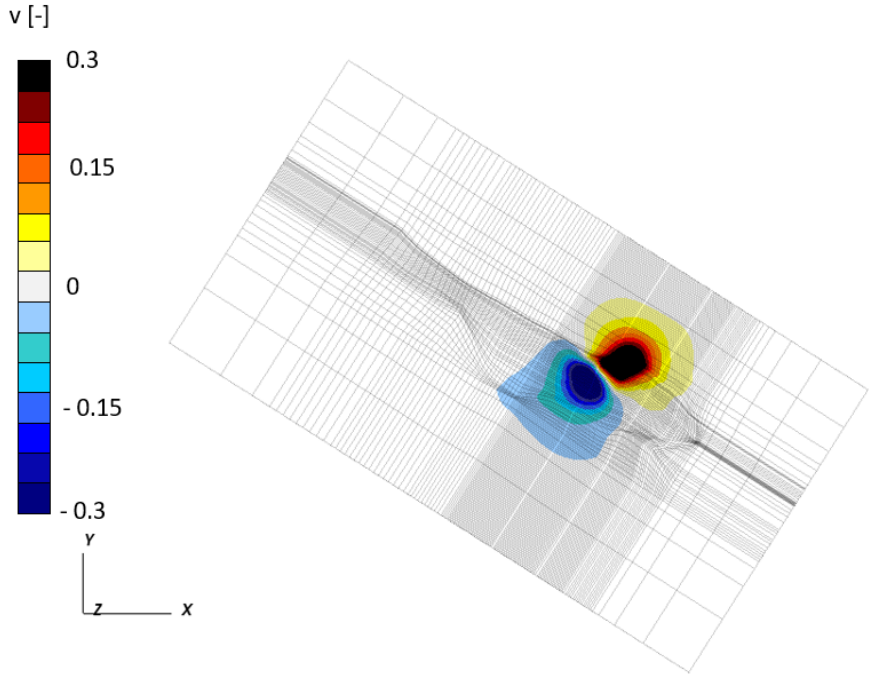

Figure 5.14: Normalized horizontal displacement v with scenario S2-P in 2022.

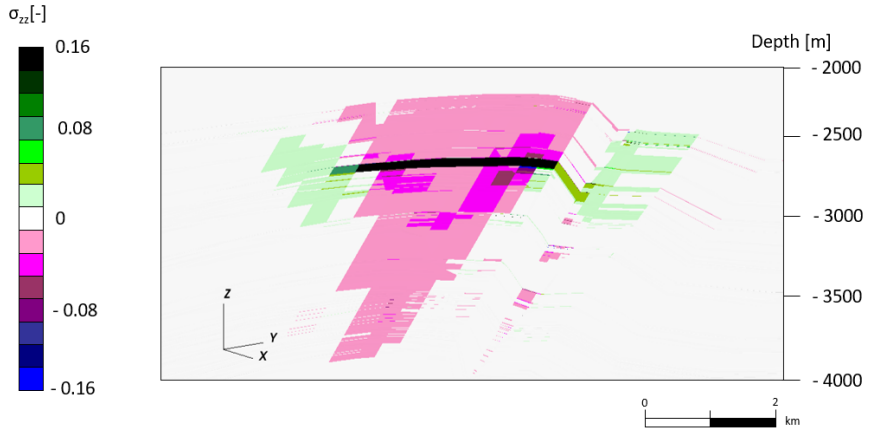

Figure 5.15: Variation of σ_{zz} between initial condition and end of the production phase in 1997 with scenario S2-P along a portion of section A-A'.

S3-P: SSCM WITH REDUCED μ^*

Scenario S3-P investigates the effect of reducing the value of μ^*. The outcomes point out a significant reduction of the maximum subsidence when compared to scenario S2-P, as expected (Fig. 5.3). Additionally, reducing this parameter limits the subsiding area, as depicted in Figs. 5.16 and 5.17, where the normalized value for vertical displacements at the end of the production phase and at the present day are shown. The comparison between the two maps allows to detect how, after the end of the actual production, the residual displacements are almost null with no rebound (as computed in scenario S1-P) or further land subsidence (as computed in scenario S2-P).

The horizontal displacements do not differ significantly from the previously discussed changes, and the results are not displayed. Similarly, also the variation of the vertical effective stress is comparable to those described for the scenario S2-P, but with smaller values.

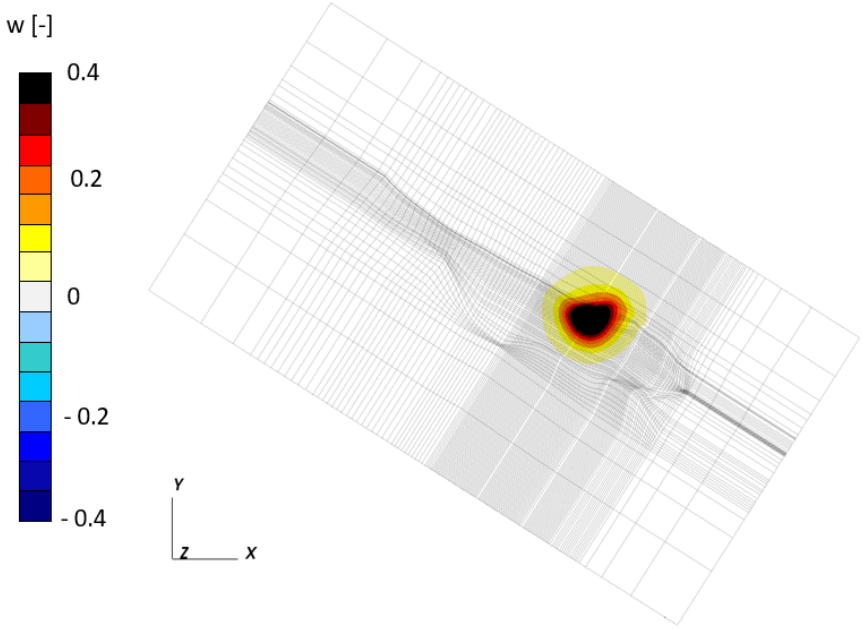

Figure 5.16: Normalized vertical displacement w with scenario S3-P at the end of the production phase in 1997.

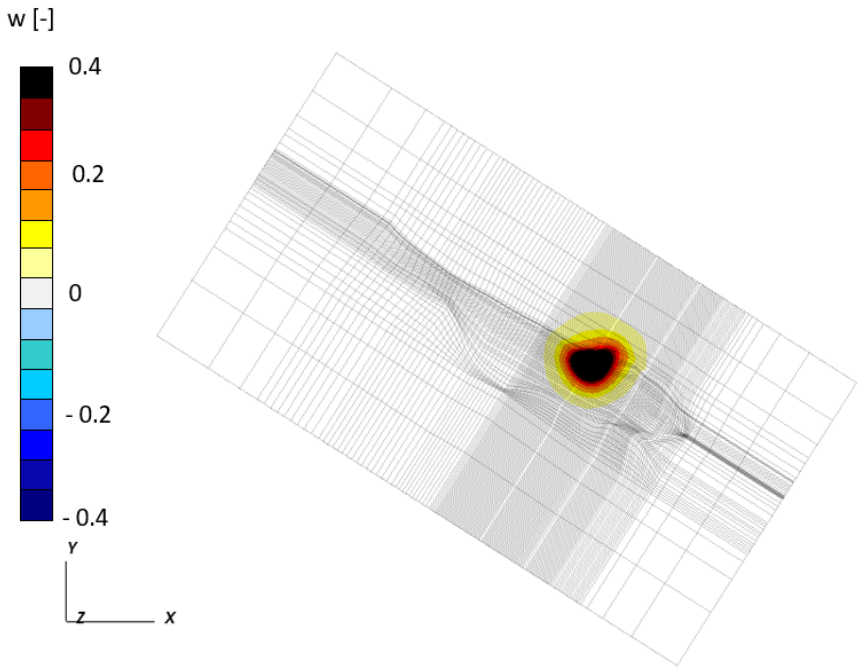

Figure 5.17: Normalized vertical displacement w with scenario S3-P in 2022.

S4-P: SSCM WITH INCREASED OCR

From the simulations carried out with an increased value of OCR (S4-P), a high stiffness of the soil can be observed. In scenario S4-P the computed displacements are even smaller than those in S1-P. This suggests that, most likely, the selected OCR value is excessively large.

The vertical displacements are provided in Fig. 5.18, showing how this case provides the smallest area affected by land subsidence. The horizontal displacements are also affected by the change in OCR, where the effect is reduced when compared to all the other simulations. Scenario S4-P, together with S1-P and S3-P, show a more linear behavior of the maximum vertical displacement versus time, with a rebound after the end of the actual production phase, which is more emphasized in S1-P and S4-P. Stress variation is also similar and more restricted when compared to S1-P, providing a resembling outcome, which for this reason is not displayed.

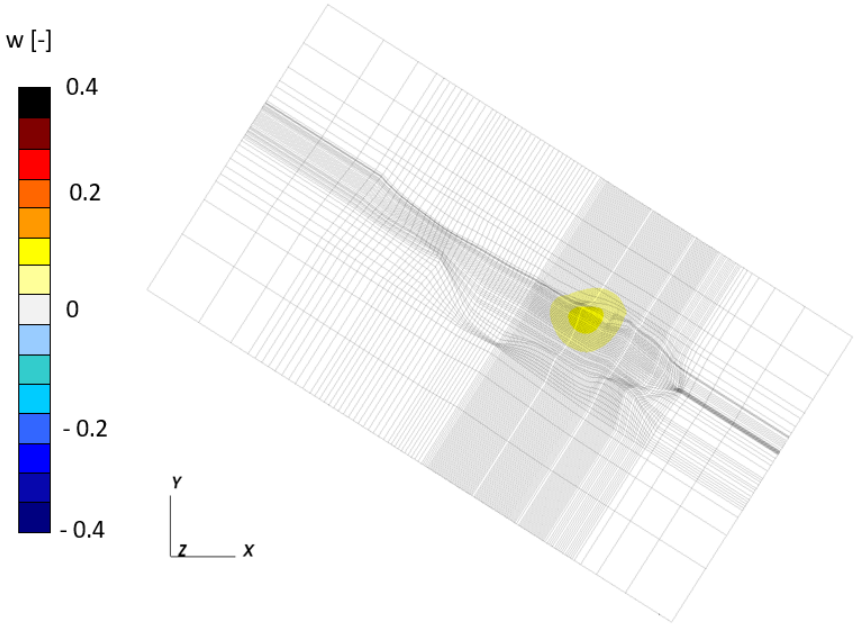

Figure 5.18: Normalized vertical displacement w with scenario S4-P at the end of the production phase in 1997.

5.2 CO_2 INJECTION

5.2.1 MODEL SET-UP

These numerical simulations foresee a two years injection of CO_2, with a constant gas injection rate and a pressure variation limited to nine cells surrounding the injection well, involving a small area as depicted in Fig. 5.19. The process leads to a constant pore pressure variation, as shown in Fig. 5.20, where the behavior versus time is represented in terms of normalized values.

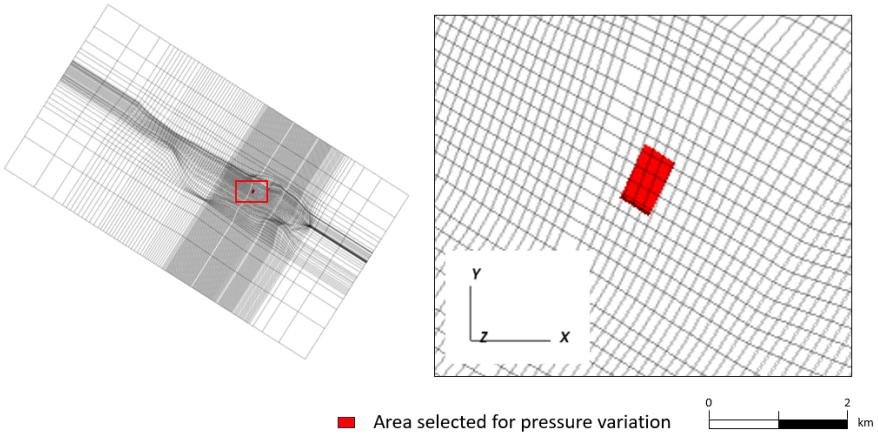

Figure 5.19: Top view close-up of the area involved by the injection of CO_2 and pressure variation.

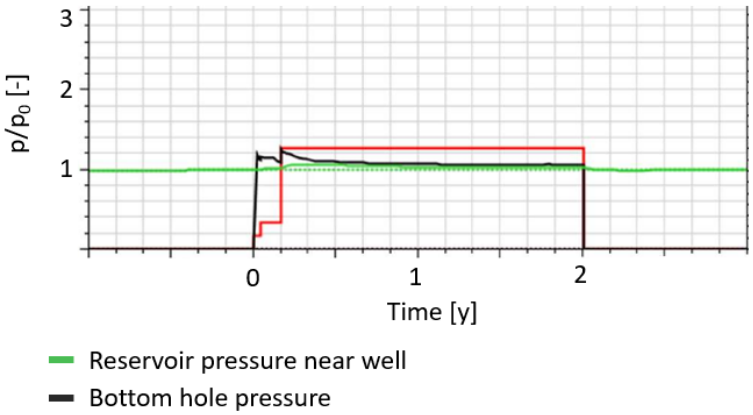

Figure 5.20: Reservoir and bottom hole normalized pressures during CO_2 injection with respect to time [years]. The gas injection rate is also highlighted in red.

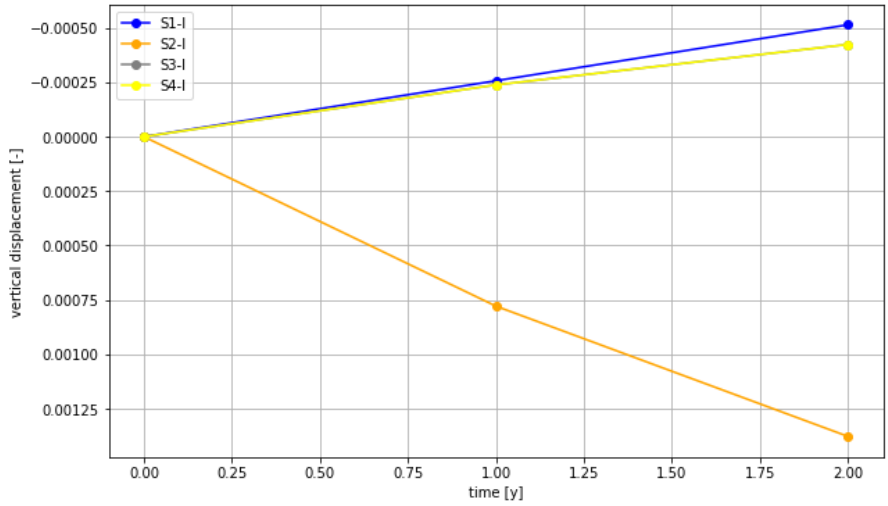

Figure 5.21: Maximum vertical displacement w over time due to CO_2 injection normalized with the largest displacement from production, scenario S2-P.

5.2.2 Results discussion

As for the simulations which describe the injection of CO_2, the results show an interesting variability in terms of relative vertical movement on the land surface, as reflected in Table 5.4. Consistently with the previous analyses, the displacement values have been normalized to the largest displacement obtained during the production phase (scenario S2-P).

TIME [y]	**1**	**2**
S1-I	-0.00026	-0.00051
S2-I	0.00078	0.00138
S3-I	-0.00024	-0.00042
S4-I	-0.00024	-0.00042

Table 5.4: Largest vertical land movement on the land surface w at the end of two years of CO_2 injection, normalized to the largest displacement computed during the production phase (scenario S2-P).

Fig. 5.21 provides the behavior versus time of the maximum normalized vertical displacement. The model computes a surface uplift with the linear elastic scenario S1-I, and the SSCM scenarios with the modified parameters (S3-I and S4-I). A certain land subsidence is still expected with the SSCM constitutive relation when the original set of parameters are accounted for (scenario S2-

I). However, notice that the movements are much smaller (about 3 orders of magnitude) than those obtained with the previous set of simulations. The negative sign means a vertical uplift of the land surface.

To make such a small displacement visible in maps and section, the bounds of the color scales have been changed with respect to the production phase simulation. For the vertical displacement w the scale has been selected between ±0.002, The visualization scales for normalized horizontal displacements u and v have also been set between ±0.0008.

In this case as well, final considerations are drawn in relation to the changes of the effective stress fields in the different simulations. The figures will show the variation normalized to the maximum initial value of stress. In light of the smaller variation, the scale has been adjusted to ±0.0005, corresponding to the largest value.

S1-I: Linear elastic

The results obtained by using a linear elastic constitutive model, drawn in blue in Fig. 5.21, show a vertical uplift of the land surface which reaches the largest value when compared to the other simulations after two years of injection. Both horizontal and vertical displacements can be observed. In Fig. 5.22 and 5.23 a top view and vertical section of the uplift at the end of the injection phase are displayed, whereas Fig. 5.24 and 5.25 depict the horizontal components along the x and y axis, respectively. The order of magnitude of these displacements has been verified using the analytical model by Geertsma, that provides the displacement field generated by a uniform pressure variation in a disk-shaped reservoir embedded in a semi-infinite uniform domain [16].

The model states that:

$$w = 2c_M h \Delta p (1 - \nu) \left(1 - \frac{d}{\sqrt{d^2 + r^2}} \right) \tag{5.1}$$

Where:

- c_M: 0.00023 MPa^{-1}, the compressibility of the volume under consideration;
- h: 67 m approximately, the height of the considered volume;
- Δp: 0.03 the change in pressure, normalized by the largest value of pressure in the reservoir;

- ν: 0.3, Poisson coefficient;
- d: 2798 m, average depth of the top of the volume;
- r: 418 m, radius of the area if it was considered to be circular, value calculated from the knowledge of the surface subject to pressure variation (550,827 m^2).

This results in:

$$w = -0.00091 \tag{5.2}$$

Where the uplift is also normalized by the largest displacement as in S2-P. This value can be compared with the displacement of -0.00051 obtained with S1-I after two years of CO_2 injection, as reported in Table 5.4. The variability in the results could, for instance, be caused by the differences between the geometry in the model and in the simulations.

Also in the injection phase, the change of the stress field remains limited to the area around the injection zone. Fig. 5.26 shows the variation in vertical effective stress σ_{zz} after two years of injection. Notice that the increase in pressure within the reservoir produces a decrease in the effective stress. The most important observation is that the stress change caused by the injection does not propagate to the fault bounding the reservoir. Hence, their initial value of the safety factor χ is not affected by the injection activity as planned in this analysis.

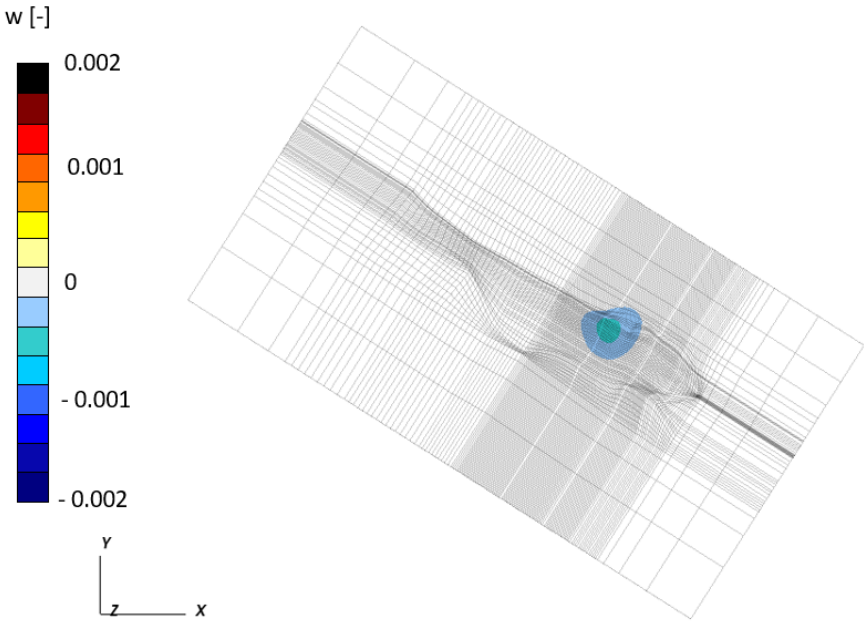

Figure 5.22: Normalized vertical displacement w as obtained with scenario S1-I after two years of CO_2 injection.

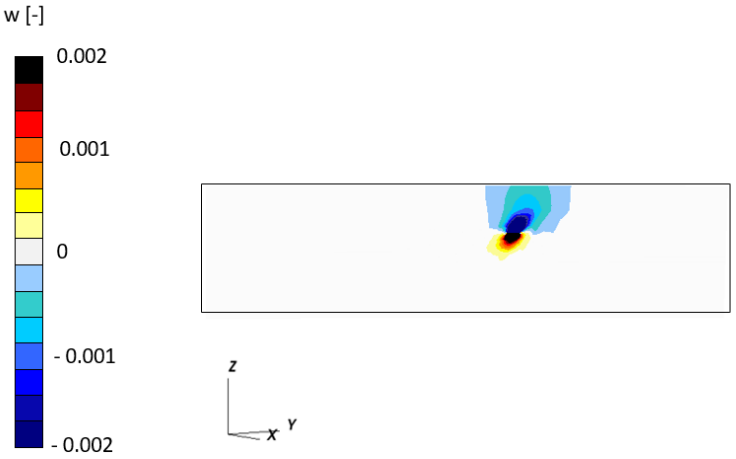

Figure 5.23: Normalized vertical displacement w along the vertical section A-A' as obtained in scenario S1-I after two years of CO_2 injection.

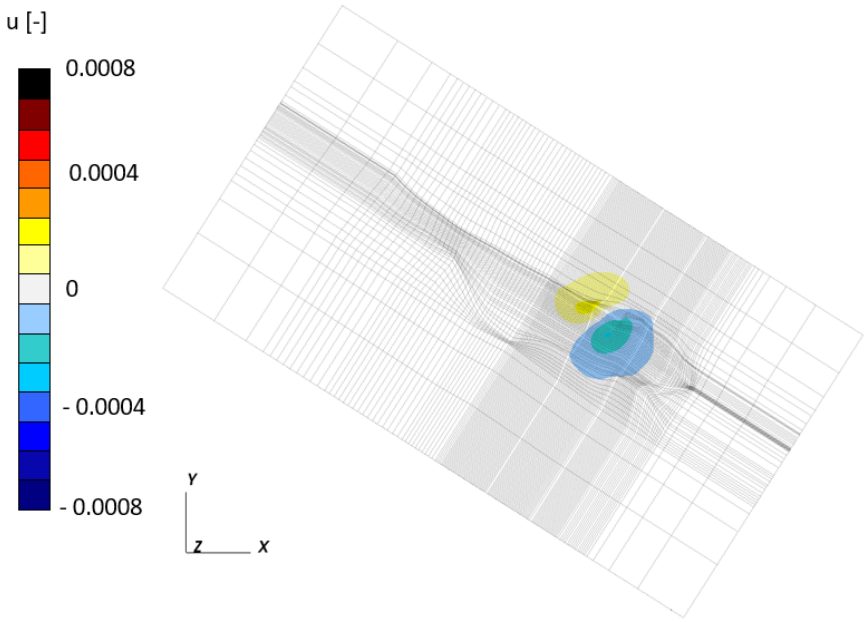

Figure 5.24: Normalized horizontal displacement u as obtained with scenario S1-I after two years of CO_2 injection.

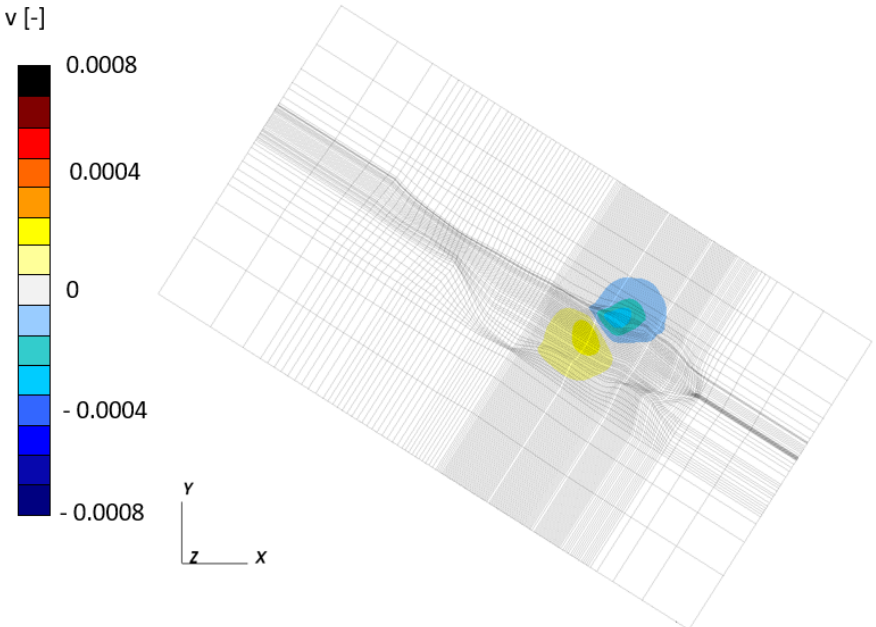

Figure 5.25: Normalized horizontal displacement v as obtained with scenario S1-I after two years of CO_2 injection.

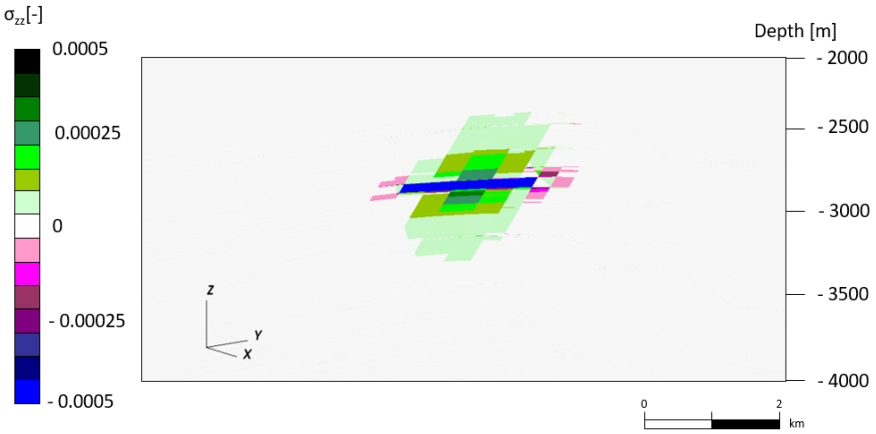

Figure 5.26: Variation of normalized σ_{zz} as obtained with scenario S1-I along the vertical section A-A′ after two years of CO_2 injection.

S2-I: SSCM

The results of the simulation in terms of maximum vertical displacement as obtained with the original SSCM constitutive model show, unexpectedly, a still ongoing subsidence also during the injection phase (Fig. 5.21). Fig 5.27, which shows the pattern of w on the land surface, helps clarifying the reason of this outcome. In fact, the entire area placed above the "reservoir material", i.e. the visco-elasto-plastic material, continues to experience a downward movement. Notice that land subsidence is minimum in the area above the cells where CO_2 is injected.

This confirms the conclusions, which are already reported in the analysis of the S2-P scenario, that the "original" values of the SSCM parameters are responsible for an excessive viscous deformation that develops over a long time range due to the soil weight.

Although physically questionable, the model outcomes in terms of horizontal displacements and change of effective stress are provided in the following for completeness.

Fig. 5.28 shows how w behaves along the A-A' vertical section through the injection elements. Fig. 5.28 also points out that a certain uplift takes place at depth above the area of injection as expected. However the uplift does not reach the land surface due to the limited areal extent of the volume experiencing the pressure increase with respect to the surrounding unit moving downward because of creep.

The pattern and magnitude of the horizontal displacements u and v are shown in Fig. 5.29 and 5.30, respectively.

The results of the effective stress variation analysis show a greater variability with respect to S1-I, but always within a consistent range of values. Fig. 5.31 shows the variation of vertical effective stress σ_{zz} between the initial condition and after two years of CO_2 injection. The pattern and values are similar to the results obtained with scenario S1-I (Fig. 5.26).

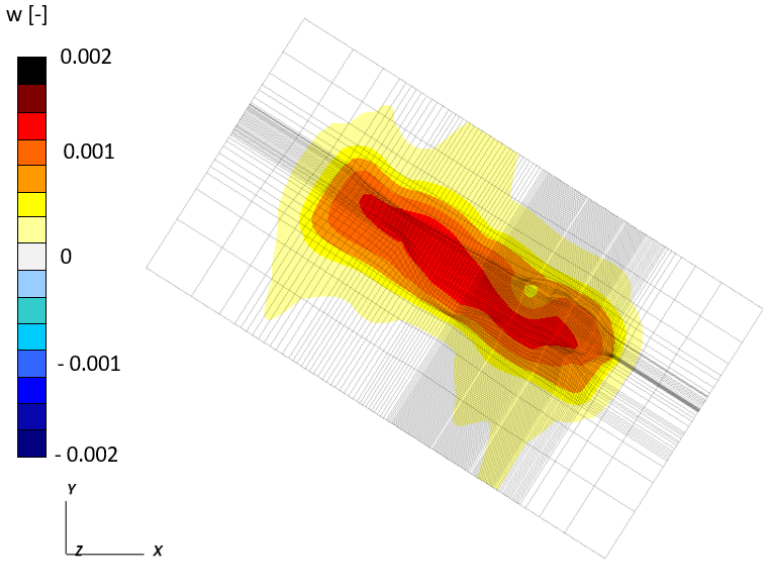

Figure 5.27: Normalized vertical displacement w as obtained with scenario S2-I after two years of CO_2 injection.

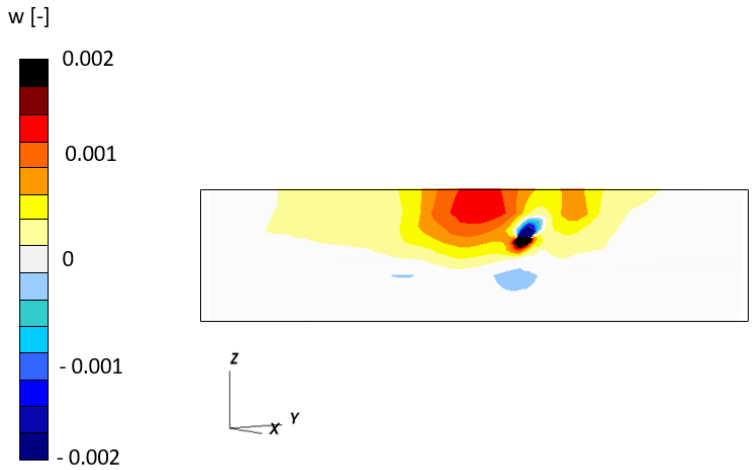

Figure 5.28: Normalized vertical displacement w along the vertical section A-A′ as obtained with scenario S2-I after two years of CO_2 injection.

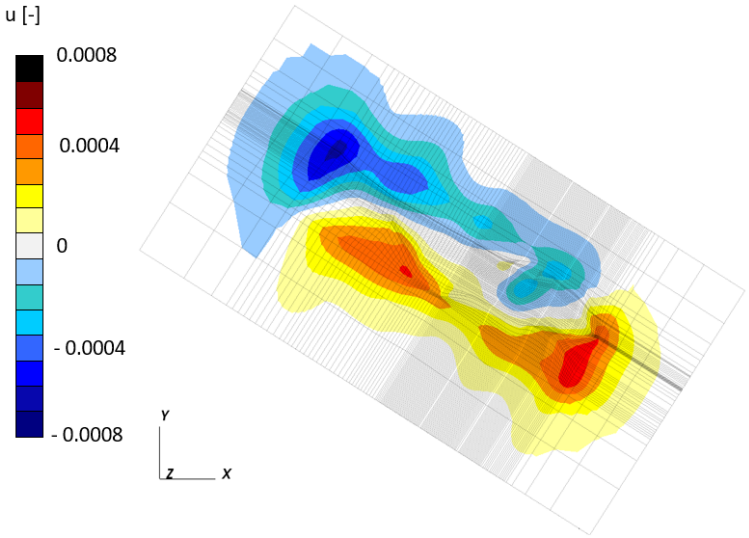

Figure 5.29: Normalized horizontal displacement u as obtained with scenario S2-I after two years of CO_2 injection.

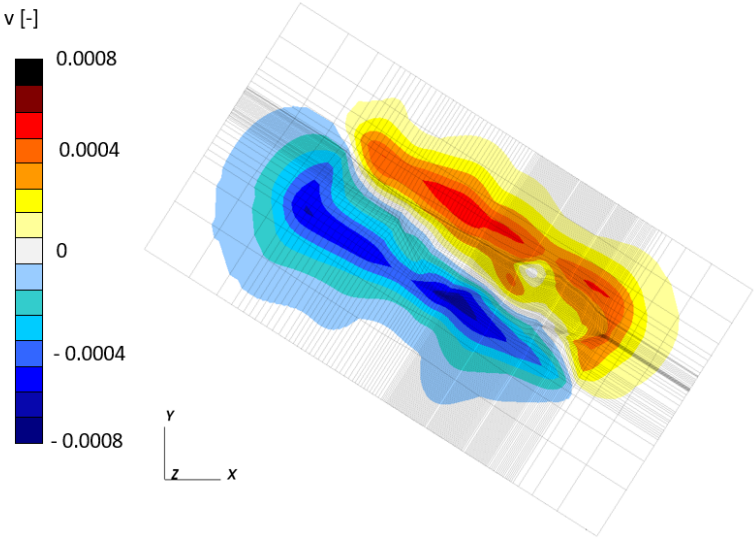

Figure 5.30: Normalized horizontal displacement v as obtained with scenario S2-I after two years of CO_2 injection.

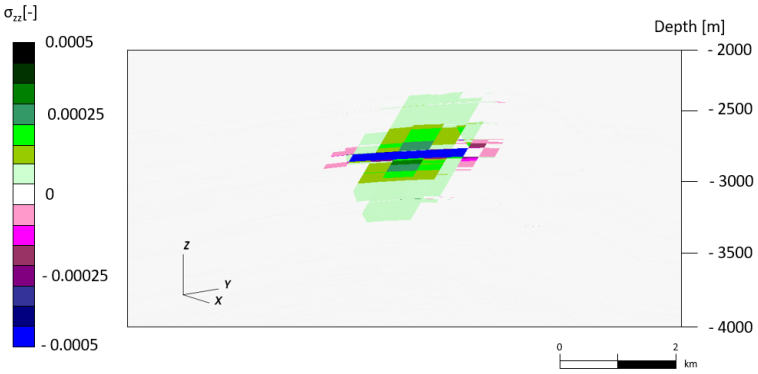

Figure 5.31: Variation of normalized σ_{zz} as obtained with scenario S2-I along the vertical section A-A′ after two years of CO_2 injection.

S3-I AND S4-I: SSCM WITH REDUCED μ^* AND INCREASED OCR

The results obtained with scenarios S3-I and S4-I based on modified values of the SSCM parameters show an almost identical trend of the maximum w versus time (Fig. 5.21). The visco-plastic contribution to the total deformation is much smaller in these scenarios and the displacements are only gently smaller than those provided by the linear elastic model. In Fig. 5.21, the grey profile related to scenario S3-I is not visible as it is completely overlapped by the yellow line relative to scenario S4-I.

Both the modifications, i.e. a reduction of μ^* or the increase of OCR, suffice to make the modeling outcome more consistent with the problem physics. The only difference that can be observed in terms of vertical displacement, is that the area where the movement occurs in S3-I is slightly larger than in S4-I, as depicted in Fig. 5.32 and 5.33, respectively. The horizontal displacements are not displayed since they resemble the outcome of scenario S1-I.

Likewise, the variation of effective stress resembles the values obtained in the other simulations and is therefore not displayed. Also in these scenarios the changes do not reach the fault systems bounding the reservoir.

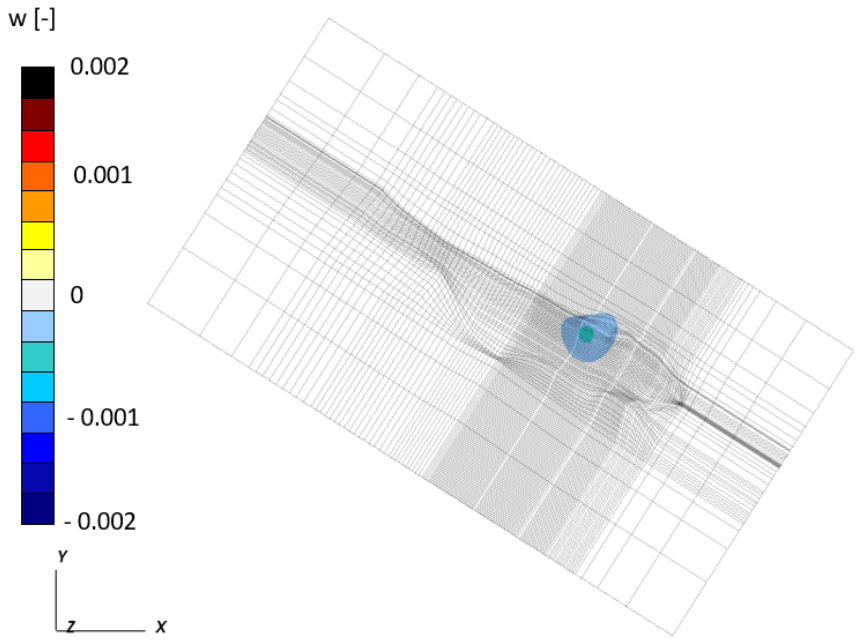

Figure 5.32: Normalized vertical displacement w as obtained with scenario S3-I after two years of CO_2 injection.

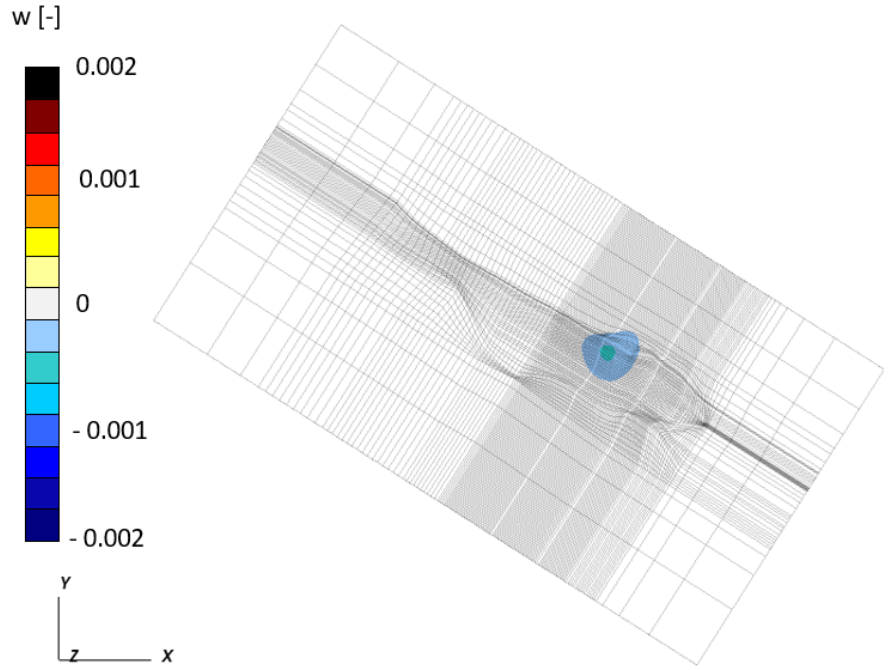

Figure 5.33: Normalized vertical displacement w as obtained with scenario S4-I after two years of CO_2 injection.

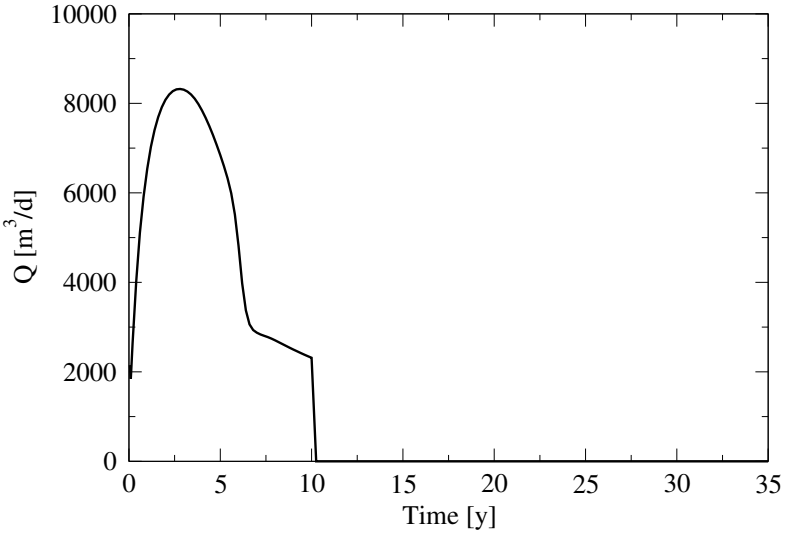

Figure 5.34: CO_2 injection rate over time as planned in scenario S1-R.

5.3 Limitations and further research

The modeling analyses presented above do not affect the fault stability because of the limited extent of the area affected by the production and CO_2 injection. As stated previously, these behaviors of the pore pressure, especially the one concerning the reservoir production, are far from being realistic. Also the CO_2 injection plan refers to a preliminary pilot intervention planned by the energy company to test the injection infrastructures. Consequently, the faults remain in their original state since the stress change develops far from the discontinuity surfaces.

A last modelling scenario carried out with a linear elastic medium (scenario S1-R in the following) has been developed to test more deeply the fault behavior in a more stressed condition. The injection rate reported in Fig. 5.34 has been simulated by the MATLAB Reservoir Simulation Toolbox (MRST) software. The injection is planned over a period of 10 years within the reservoir layers in the depth range between 4200 and 4600 m below sea level. The behavior of the average reservoir pore pressure versus time is shown in Fig. 5.35. The pressure increases by approximately 5.7 MPa during the 10-year injection period and remains constant afterward.

The volume affected by the pressure change is highlighted in Fig. 5.36.

The pressure variation has been used as input data to the geomechanical simulator. The outcomes in terms of displacement distribution are interesting

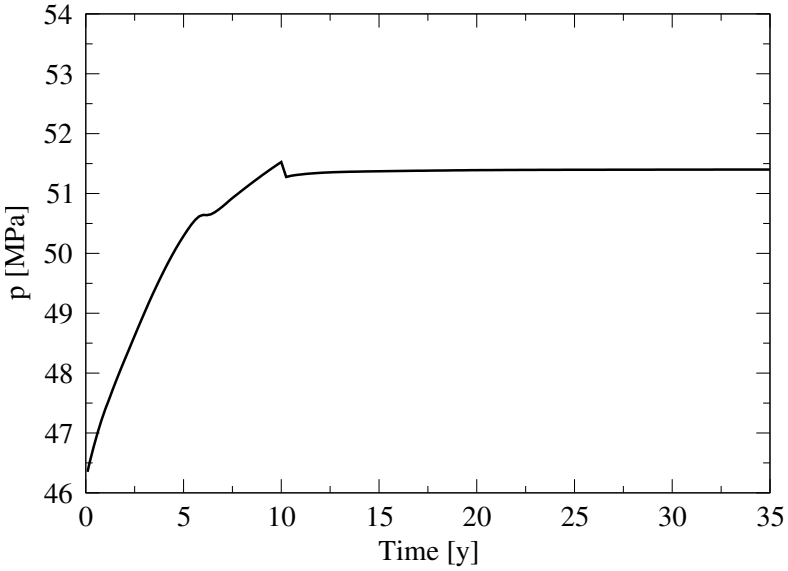

Figure 5.35: Pressure behavior over time as planned in the scenario S1-R.

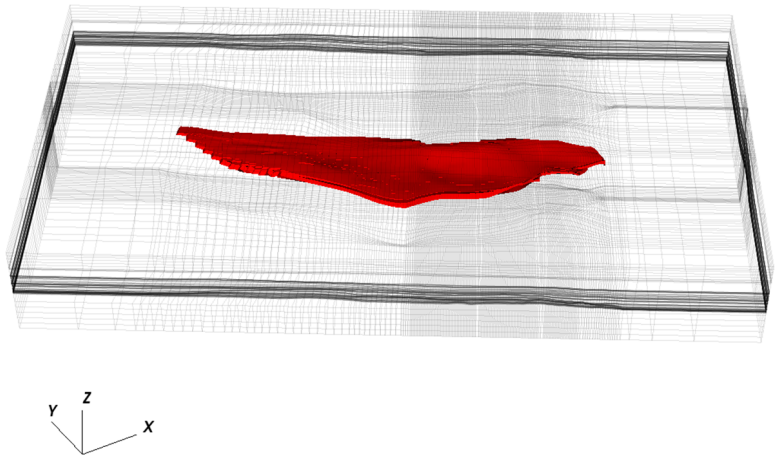

Figure 5.36: Volume experiencing a pressure variation due to injection of CO_2 as obtained in scenario S1-R.

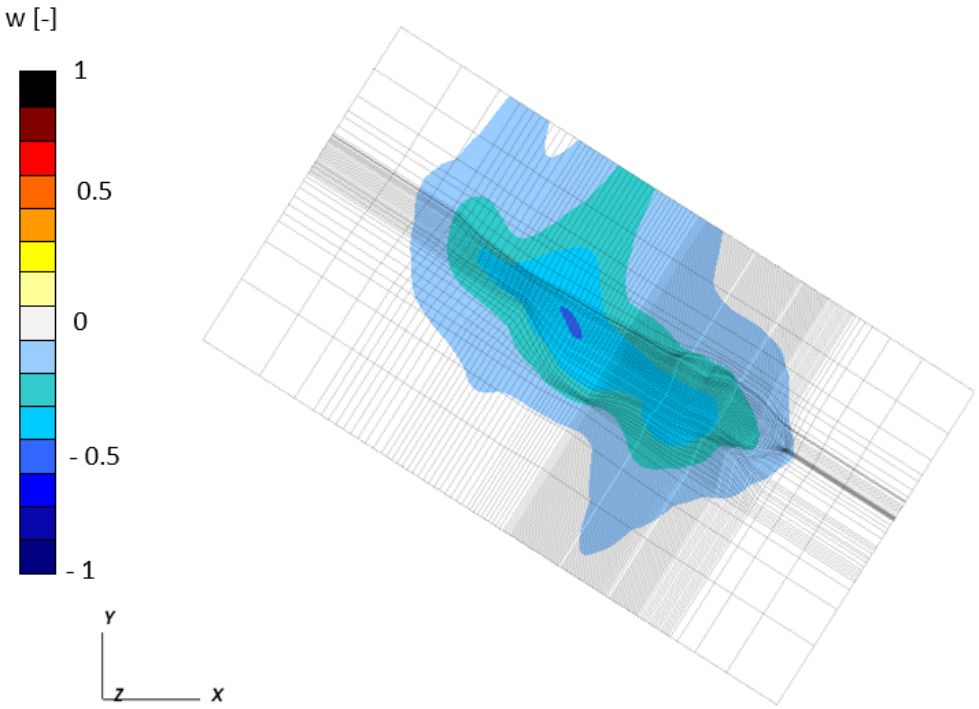

Figure 5.37: Normalized vertical displacement w as obtained with scenario S1-R after ten years of CO_2 injection.

and meaningful. As an example, Fig. 5.37 shows the simulated land uplift at the end of the injection period, normalized by the largest displacement obtained in the previous scenarios.

However, once the IEs are inserted to investigate the possible fault activation, the nonlinear model does not converge. This unexpected problem has been experienced independently of the number of faults inserted in the domain. Previous experiences showed that model convergence is challenging when several faults are introduced in the discretization due to the model complexity, but it is when one or two discontinuities are included at the same time.

An in-depth analysis has been carried out to understand the reason for such an anomalous behavior of the GEPS3D simulator. It has been clarified that it is related to the 3D mesh features, and specifically to the element shape. Fig. 5.38 shows a portion of the mesh corresponding to the reservoir layers. The elements are characterized by a horizontal characteristic dimension on the order of 100 m, but the thickness, i.e. the dimension along the vertical dimension, reduces to approx 1 m only. The element distortion is really high, causing an extremely poor quantification of the stress changes, which are computed as partial derivatives

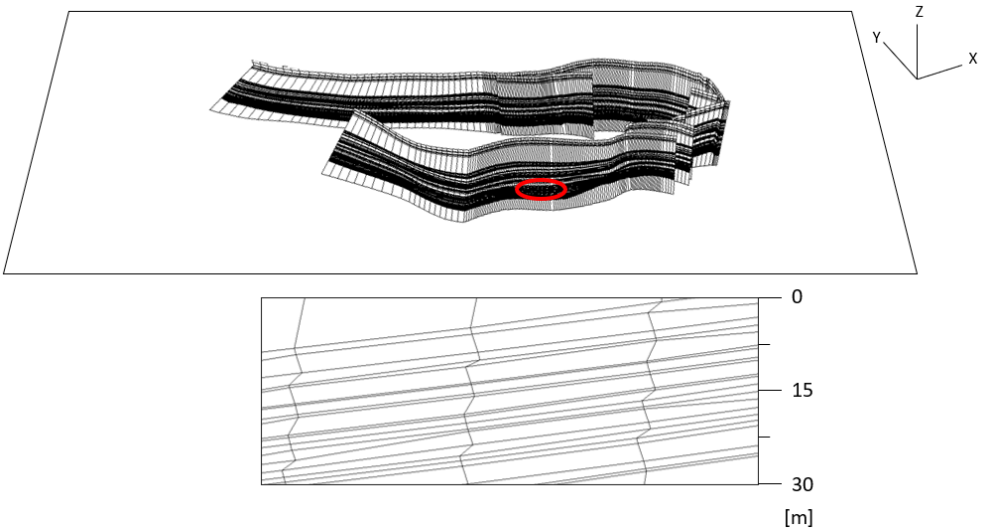

Figure 5.38: System of faults and detail of the mesh discretization at the reservoir depth.

of the displacement values at the element nodes (see Section 2.2). Because of this, also the small displacements computed after one time step of CO_2 injection are responsible for nonphysical huge picks of stress variation in the nearby of the faults, which largely activate everywhere causing the model failure.

Further improvements, if the mesh is meant to also embody important non-linearities such as faults, would require the processing of a new 3D grid. Concluding, the analysis has allowed to point out the inappropriateness of the 3D mesh provided by the energy company to perform geomechanical investigations with a discontinuous medium, i.e. when the domain is intersected by faults for which a failure analysis must be developed.

6

Conclusions

The withdrawal or sequestration of fluids, such as CO_2, from / into underground reservoirs should properly address and take into consideration geomechanical aspects. These topics are fundamental in relation to the assessment of the storage capacity of the site with respect to the safety of the injection/production processes. Some of the most important issues to consider are land displacement, shear or tensile failure of the reservoir caprock, and the possible re-activation of existing faults crossing the formation.

In this thesis, the displacements and stress changes caused by the primary production and CO_2 injection from/in a deep geological reservoir in the Adriatic offshore are simulated by the geomechanical simulator GEPS3D, using a Finite Element method.

By applying an uncoupled approach, the estimated pressure field is initially quantified and then used as input for the geomechanical model. The model has been tested by performing a parametric analysis, considering a set of constitutive relationships to describe the mechanical behavior of the reservoir formation. A simple linear elastic relationship has been initially used (S1), and the outcomes are then compared with those obtained by a soft-soil creep model (S2). Furthermore, the SSCM parameters provided by the energy company have been varied by reducing the viscosity (S3) or increasing the overconsolidation ratio (S4) to test the model sensitivity.

The results of this parametric analysis show a considerable variability in the outcomes of the simulations. During the production, the largest vertical and horizontal displacements are obtained in the S2 simulations, with land

subsidence that is computed also after the end of the production phase when the reservoir pressure recovers. Land displacements during a 2-year CO_2 injection phase are much smaller than those computed during the primary production. The use of linear elastic law (S1) predicts the largest vertical uplift and the largest horizontal displacements. The small injected amount is also reflected in a limited variation of the effective stress field. On the other hand, the scenario based on SSCM provides land subsidence also during the injection phase. This nonphysical behavior is caused by the creep deformation of the reservoir due to its own weight.

These considerations suggest that the original parameters used in the SSCM are responsible for an excessive creep. Their adjustment has allowed to achieve more physical outcomes in terms of land displacements.

Another important outcome of the thesis refers to the 3D mesh provided by the energy company and used for the geomechanical simulations. In fact, it was not possible to investigate the possible activation of the fault system surrounding and crossing the reservoir due to the geometry of the grid that is made of elements with a huge distortion between the horizontal and vertical directions. Their dimension amounts to about 100 m along the East-West and South-North directions and about 1 m along the vertical one. This causes a huge inaccuracy in the numerical computation of the stress field, with the calculation of unrealistic stress changes on the discontinuity planes and the failure of the model convergence.

Therefore, the 3D grid should be re-built to allow a more accurate analysis of the safety condition of the fault system, and consequently the safety of the geologic sequestration, following massive CO_2 injection. Regarding a pilot experiment of CO_2 injection, which will cause a limited pressure increase in a small reservoir portion quite far from the faults, the modeling outcome has excluded any change of the stress regime on the faults and a limited movement of the land surface.

References

[1] Juan Carlos Abanades et al. "Summary for policymakers, concerning current understanding of carbon dioxide capture and storage." In: (2005). URL: https://www.ipcc.ch/site/assets/uploads/2018/03/srccs_summaryforpolicymakers-1.pdf.

[2] Sally Benson et al. "Underground geological storage". In: (2005). URL: https://www.ipcc.ch/report/carbon-dioxide-capture-and-storage/underground-geological-storage/.

[3] Maurice A Biot. "General theory of three-dimensional consolidation". In: *Journal of applied physics* 12.2 (1941), pp. 155–164.

[4] Wenzhuo Cao et al. "Evaluation of shear slip stress transfer mechanism for induced microseismicity at In Salah CO2 storage site". In: *International Journal of Greenhouse Gas Control* 107 (2021), p. 103302. ISSN: 1750-5836. DOI: https://doi.org/10.1016/j.ijggc.2021.103302.

[5] Nicola Castelletto, G. Gambolati, and P. Teatini. "Geological CO_2 sequestration in multi-compartment reservoirs: Geomechanical challenges: CO_2 SEQUESTRATION IN FAULTED RESERVOIRS". In: *Journal of Geophysical Research: Solid Earth* 118.5 (May 2013), pp. 2417–2428. ISSN: 21699313. DOI: 10.1002/jgrb.50180. URL: http://doi.wiley.com/10.1002/jgrb.50180.

[6] Nicola Castelletto et al. "Can natural fluid pore pressure be safely exceeded in storing gas underground?" In: *Engineering Geology* 153 (Feb. 2013), pp. 35–44. ISSN: 00137952. DOI: 10.1016/j.enggeo.2012.11.008.

[7] Council of European Union. *Council regulation (EU) no 869/2022*. https://eur-lex.europa.eu/legal-content/EN/TXT/PDF/?uri=CELEX:32022R0869. 2022.

[8] Tim Dixon and Andrew Birchenough. "Exporting CO2 for Offshore Storage–The London Protocols Export Amendment". In: *Proceedings of the 15th Greenhouse Gas Control Technologies Conference*. 2021, pp. 15–18.

[9] Marco Favaretti. *Geotechnical Engineering Textbook*. University Lecture, Environmental Geotechnics. 2022.

[10] Massimiliano Ferronato et al. "Geomechanical issues of anthropogenic CO2 sequestration in exploited gas fields". In: *Energy Conversion and Management* 51.10 (Oct. 2010), pp. 1918–1928. ISSN: 01968904. DOI: 10.1016/j.enconman.2010.02.024.

[11] Massimiliano Ferronato et al. "Numerical modelling of regional faults in land subsidence prediction above gas/oil reservoirs". In: *International Journal for Numerical and Analytical Methods in Geomechanics* 32.6 (Apr. 25, 2008), pp. 633–657. ISSN: 03639061, 10969853. DOI: 10.1002/nag.640.

[12] Andrea Franceschini et al. "A novel Lagrangian approach for the stable numerical simulation of fault and fracture mechanics". In: *Journal of Computational Physics* 314 (June 2016), pp. 503–521. ISSN: 00219991. DOI: 10.1016/j.jcp.2016.03.032.

[13] Andrea Franceschini et al. "Unexpected fault activation in underground gas storage. Part I: Mathematical model and mechanisms". In: *arXiv preprint arXiv:2308.02198* (2023).

[14] Giuseppe Gambolati, P Gatto, and G Ricceri. "Land subsidence due to gas/oil removal in layered anisotropic soils by a finite element model". In: *Proceedings of the Third International Symposium on Land Subsidence, IAHS Publ*. Vol. 151. 1984, pp. 29–41.

[15] Giuseppe Gambolati et al. "Importance of poroelastic coupling in dynamically active aquifers of the Po river basin, Italy". In: *Water Resources Research* 36.9 (2000), pp. 2443–2459.

[16] J Geertsma. "Land subsidence above compacting oil and gas reservoirs". In: *Journal of petroleum technology* 25.06 (1973), pp. 734–744.

[17] Hasan Gercek. "Poisson's ratio values for rocks". In: *International Journal of Rock Mechanics and Mining Sciences* 44.1 (2007), pp. 1–13.

[18] Richard E Goodman, Robert L Taylor, and Tor L Brekke. "A model for the mechanics of jointed rock". In: *Journal of the soil mechanics and foundations division* 94.3 (1968), pp. 637–659.

[19] *IEA, CO2 transport and storage*. https://www.iea.org/reports/co2-transport-and-storage.

[20] Giovanni Isotton et al. "Robust numerical implementation of a 3D rate-dependent model for reservoir geomechanical simulations". In: *International Journal for Numerical and Analytical Methods in Geomechanics* 43.18 (Dec. 25, 2019), pp. 2752–2771. ISSN: 0363-9061, 1096-9853. DOI: 10.1002/nag.3000.

[21] Hoesung Lee et al. "AR6 Synthesis Report: Climate Change 2023". In: (2023). URL: https://report.ipcc.ch/ar6syr/pdf/IPCC_AR6_SYR_LongerReport.pdf.

[22] YH Li, RP Niu, and GR Liu. "Highly accurate smoothed finite element methods based on simplified eight-noded hexahedron elements". In: *Engineering Analysis with Boundary Elements* 105 (2019), pp. 165–177.

[23] Pascal Longuemare et al. "Geomechanics in reservoir simulation: overview of coupling methods and field case study". In: *Oil & gas science and technology* 57.5 (2002), pp. 471–483.

[24] Mimmo Palano et al. "Geopositioning time series from offshore platforms in the Adriatic Sea". In: *Scientific Data* 7.1 (2020), p. 373.

[25] Jonny Rutqvist, JT Birkholzer, and Chin-Fu Tsang. "Coupled reservoir–geomechanical analysis of the potential for tensile and shear failure associated with CO2 injection in multilayered reservoir–caprock systems". In: *International Journal of Rock Mechanics and Mining Sciences* 45.2 (2008), pp. 132–143.

[26] Jonny Rutqvist, Donald W Vasco, and Larry Myer. "Coupled reservoir-geomechanical analysis of CO2 injection and ground deformations at In Salah, Algeria". In: *International Journal of Greenhouse Gas Control* 4.2 (2010), pp. 225–230.

[27] Matt Steyn et al. "GLOBAL STATUS OF CCS 2022". In: (2022). URL: https://www.globalccsinstitute.com/resources/global-status-of-ccs-2022/.

[28] Pietro Teatini. *3D Geomechanics*. University Lecture, Underground Fluids, Energy and Environment. 2021.

[29] Pietro Teatini, Nicola Castelletto, and Giuseppe Gambolati. "3D geomechanical modeling for CO2 geological storage in faulted formations. A case study in an offshore northern Adriatic reservoir, Italy". In: *International Journal of Greenhouse Gas Control* 22 (Mar. 2014), pp. 63–76. ISSN: 17505836. DOI: 10.1016/j.ijggc.2013.12.021.

[30] Pietro Teatini et al. "Geomechanical response to seasonal gas storage in depleted reservoirs: A case study in the Po River basin, Italy: GEOMECHANICAL RESPONSE TO SEASONAL GAS STORAGE". In: *Journal of Geophysical Research: Earth Surface* 116 (F2 June 2011). ISSN: 01480227. DOI: 10.1029/2010JF001793.

[31] Pietro Teatini et al. "MODELING INDUCED SEISMICITY BY GAS PRODUCTION AND STORAGE IN FAULTED SEDIMENTARY RESERVOIRS". In: ().

[32] Kok Sien Ti et al. "A review of basic soil constitutive models for geotechnical application". In: *Electronic Journal of Geotechnical Engineering* 14 (2009), pp. 1–18.

[33] PA Vermeer and HP Neher. "A soft soil model that accounts for creep". In: *Beyond 2000 in computational geotechnics* (1999), pp. 249–261.